

**A Ground-Up Data-Driven Approach to Distinguishing Magnetospheric Sources of Geomagnetically  
Induced Currents > 10 A during the 17 March 2013 Event**

**Bhagyashree Waghule<sup>1</sup>, D.J. Knipp<sup>1</sup>, J. L. Gannon<sup>2</sup>, D. Billet<sup>3</sup>, S.K. Vines<sup>4</sup>, J. Goldstein<sup>5</sup>**

<sup>1</sup>University of Colorado Boulder.

<sup>2</sup>Computational Physics Inc.

<sup>3</sup>University of Saskatchewan

<sup>4</sup>Johns Hopkins University Applied Physics Laboratory

<sup>5</sup>Southwest Research Institute

*Corresponding author: Bhagyashree Waghule (bhagyashree.waghule@colorado.edu)*

**Key Points:**

- Wavelet analysis of GICs at Mäntsälä on 17 March 2013 reveals two features – Pi1/Pi2 pulsations superposed on longer duration disturbances.
- Wavelet decomposition of the GIC and BH signals is consistent with multi-scale magnetosphere-ionosphere activity around GIC spikes.
- Pi2 pulsations and data fusion suggest mesoscale flow channels (substorm injections) were the underlying cause of four GICs > 10 A.

## Abstract

We combine wavelet analysis and data fusion to investigate geomagnetically induced currents (GICs) on the Mäntsälä pipeline and the associated horizontal geomagnetic field,  $B_H$ , variations during the late main phase of the 17 March 2013 geomagnetic storm. The wavelet analysis decomposes the GIC and  $B_H$  signals at increasing ‘scales’ to show distinct multi-minute spectral features around the GIC spikes. Four GIC spikes  $> 10$  A occurred while the pipeline was in the dusk sector – the first sine-wave-like spike at  $\sim 16$  UT was ‘compound.’ It was followed by three ‘self-similar’ spikes two hours later. The contemporaneous multi-resolution observations from ground-(magnetometer, SuperMAG, SuperDARN), and space-based (AMPERE, TWINS) platforms capture multi-scale activity to reveal two magnetospheric modes causing the spikes. The GIC at  $\sim 16$  UT occurred in two parts with the negative spike associated with a transient sub-auroral eastward electrojet that closed a developing partial ring current (PRC) loop, whereas the positive spike developed with the arrival of the associated mesoscale flow-channel in the auroral zone. The three spikes between 18-19 UT were due to bursty bulk flows (BBFs). We attribute all spikes to flow-channel injections (substorms) of varying scales. We use previously published MHD simulations of the event to substantiate our conclusions, given the dearth of timely in-situ satellite observations. Our results show that multi-scale magnetosphere-ionosphere activity that drives GICs can be understood using multi-resolution analysis. This new framework of combining wavelet analysis with multi-platform observations opens a research avenue for GIC investigations and other space weather impacts.

## **Plain Language Summary**

Geomagnetically Induced Currents (GIC) are produced by complex interaction between the Earth's magnetic field and ground composition during intense geomagnetic storms. These two parameters are often related in frequency domain. In this paper, we analyze the GIC signal from the Finnish natural gas pipeline recorded at Mäntsälä during the 17 March 2013 geomagnetic storm. Four spikes  $> 10$  Ampere were recorded between 4:30 – 9:00 PM local time. We use wavelet analysis to learn about the frequencies of GIC spikes and then systematically investigate the observations from ground to space (ground-up approach) to learn what links activity in space to the GICs. Wavelet analysis highlights areas ranging from  $<1$  minute to  $> 30$  minutes, which indicates that higher frequency fluctuations are accompanied with longer duration disturbance. Multi-platform observations help us interpret the physical meaning of the multi-minute (or multi-scale) area in the wavelet plot. We find that multi-scale activity in the magnetosphere and ionosphere, created by fast earthward- flowing particles (magnetotail mesoscale plasma flows), ultimately drove the significant GIC spikes. This new perspective enabled us to link the magnetospheric activity to GICs through observations and previously published simulations and pave a path for future research.

## 1. Introduction

Geomagnetically induced currents (GICs) flow near the Earth's surface because of induced geoelectric field. The geoelectric field is related to the magnetic field and ground conductivity in the frequency domain such that the product of frequency spectrum of the northward (southward) magnetic field (**B**) component and the transfer function of the Earth produce the frequency spectrum of the eastward (westward) geoelectric field which drives GICs (Boteler, 1994). Eventually, GICs find a path to close the circuit through long conductive systems (>1km) such as power lines, pipelines, and communication cables, which pose a significant risk to technological infrastructure (Pulkkinen et al., 2017). Hence, understanding the drivers of GICs at different timescales is essential for accurate predictions. Tsurutani & Hajra (2021) surveyed the solar wind conditions for GICs > 10 A in the Mäntsälä pipeline and recommended a deeper investigation into the related near-Earth interactions. Herein, we employ wavelet analysis to decompose the GIC and the horizontal **B** component (BH) time-series at different scales (frequencies). The combined information from wavelet analysis and data fusion of multi-resolution ground and space-based observations is used to explore the magnetospheric source(s) of four GIC spikes (>10 A) recorded at Mäntsälä station of the Finnish natural gas pipeline network, during the CME passage of the 17 March 2013 geomagnetic storm. Although not among the extreme events studied by Juusola et al. (2023), this storm is interesting because wavelet analysis suggests distinct GIC responses to different drivers. We hypothesize that the first GIC spike had a compound source primarily associated with the interplay between partial ring current (PRC), plasmopause, and substorm injection (mesoscale plasma flows), while the other spikes are associated with bursty bulk flow (BBF).

Our analysis is informed by prior GIC studies and recent modeling efforts for the event. W.-H. Xu et al. (2022) established the utility of wavelet analysis as a tool for analyzing the 17

81 March 2013 Mäntsälä GICs, relating them to the rate of change of the x-component geomagnetic  
82 field ( $dB_x/dt$ ) signal at a reference ground magnetometer at Nurmijärvi, but did not address their  
83 causes. Belakhovsky et al. (2019) noted very intense ionospheric vortex-driven GICs in  
84 transformers in the Kola Peninsula, north of Mäntsälä during the storm. These spikes were  
85 attributed to large-amplitude magnetic pulses that appeared to be part of a nightside substorm  
86 current wedge (SCW). Despirak et al. (2022) also studied disturbances on the Karelian-Kola  
87 power transmission line for the same date, finding that GICs corresponded to the appearance of  
88 successive substorm intensifications.

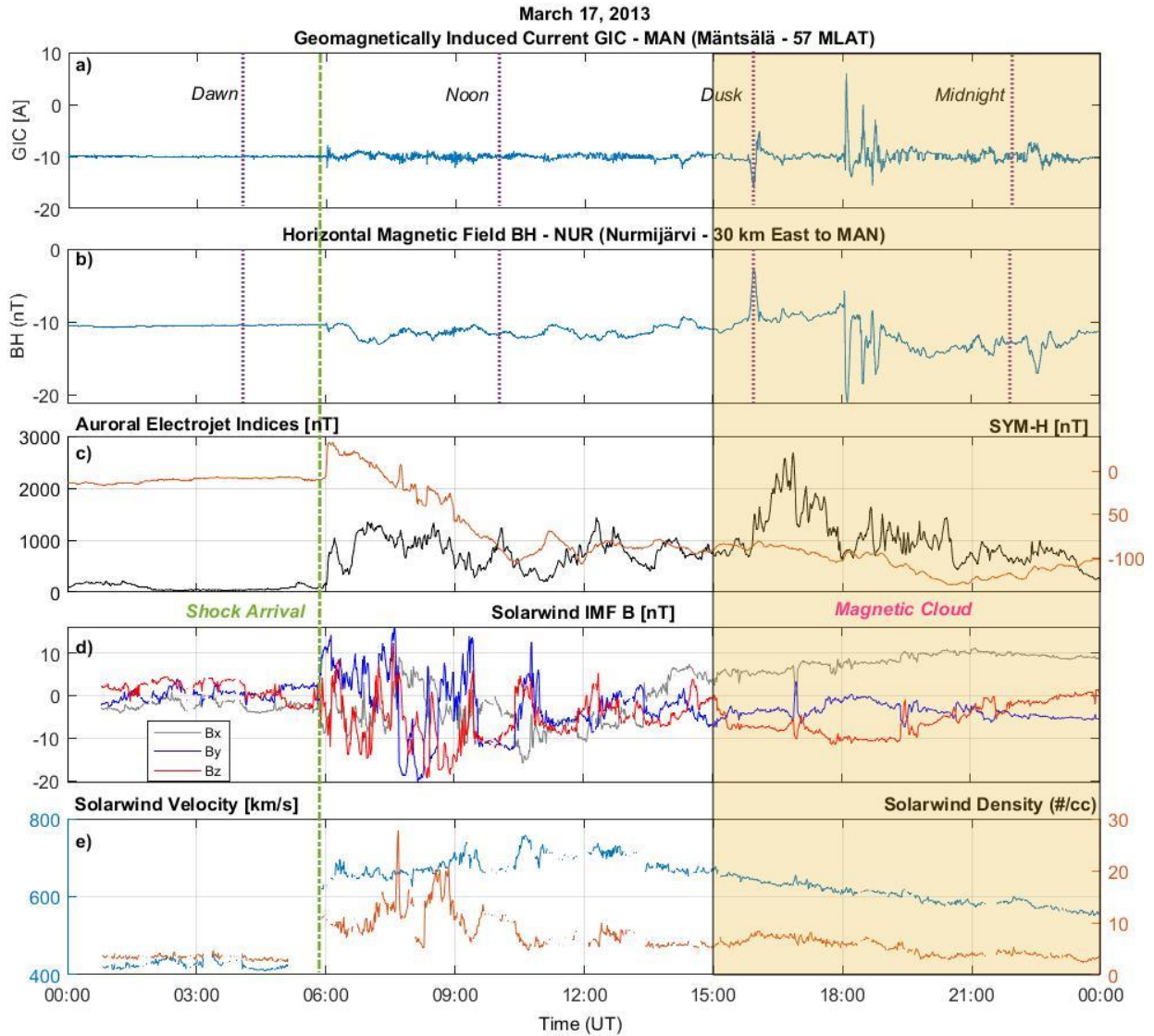


**Figure 1:** a) GIC at Mäntsälä; b) BH at Nurmijärvi ~ 30 km east of Mäntsälä; c) Global Auroral Electrojet index and SYM-H index; d) IMF components; e) Solar wind density and velocity. Pink lines denote (Magnetic) local time at Mäntsälä (approximately UT+2h). Green line indicates shock arrival, and the highlighted yellow region indicates interval of magnetic cloud.

Figure 1 provides a ground-to-space view of activity during the 2013 St Patrick's Day storm. A sudden change in GIC and BH (Fig. 1a-b) and global auroral and RC activity (Fig. 1c) occurred at ~06 UT, simultaneous with the arrival of a solar wind shock indicated by an increase in interplanetary magnetic field (IMF) fluctuations (Fig. 1d) and increased solar wind speed and

density (Fig. 1e). During the post-shock interval (06-15 UT) an intense,  $Dst < 100$  nT, geomagnetic storm developed (Fig. 1c) with significant increases in substorm activity and magnetosphere-ionosphere (M-I) coupling (e.g., Lyons et al., 2016). Despite the post-shock IMF and solar wind variations, the Mäntsälä pipeline experienced only small GICs while it transited the dayside. Verkhoglyadova et al. (2016) and Wu et al. (2016) noted that the IMF stabilized as the leading edge of a magnetic cloud (MC) arrived at ~15:30 UT, after which the IMF was southward. Four GIC spikes arose while the pipeline moved through the duskside (Fig. 1a). A sinusoid-shaped spike at ~16 UT was associated with a sharp increase in BH (Fig.1b) while the other three GIC spikes between 18-19 UT were associated with sharp dips in BH. This interval in the late main phase/recovery phase of the storm has been well studied in context of nightside activity (e.g., Gkioulidou et al., 2014 and Yu et al., 2014)

The understanding of magnetospheric dynamics has improved over time through MHD simulations such as those applied in Multiscale Atmosphere-Geospace Environment (MAGE) efforts. Wiltberger et al. (2017) showed an increased plasma pressure in the duskside magnetosphere within  $4R_E$ . Sorathia et al. (2018), showed peak electron injection at 16 UT followed by ion injections in the recovery phase of the storm. Later, Sorathia et al. (2023) identified plasmashet mesoscale bubbles that penetrate the inner magnetosphere, as an early multi-scale source of the auroral electrojet and  $dB/dt$  variations on the ground. Their findings are supplemented by Sciola et al. (2023) who show that bubbles are responsible for at least 50% of the plasma energy enhancement within  $6 R_E$  during this strong geomagnetic storm. We note that advances in simulations have been instrumental in associating terms like mesoscale plasma flow, ionization channels, plasma bubbles and bursty bulk flows with substorm and RC injection.

Our motivating question is - How would wavelet analysis help with understanding the magnetospheric drivers of the GIC spikes? The frequency of magnetic field perturbations is important for generating GICs because longer-period fluctuations penetrate more deeply into the Earth, whereas the short-period fluctuations remain closer to the surface (Gannon et al., 2017). Hence, compared to a 1-D time series, a 2-D time-frequency analysis (such as wavelet transform) aids in understanding the distribution of fluctuations in the GIC signal and the associated BH fluctuations.

Wavelet analysis has been used in climate studies to understand periodic behavior (Yiou et al., 1996; Torrence & Compo, 1998 and references therein), and to understand geophysical time-series (Grinsted et al., 2004). Pulkkinen & Kataoka (2006) used the S-transform method to study the properties of GIC fluctuations in the Finnish natural gas pipeline. Later, Z. Xu (2011) reported that wavelet analysis could distinguish geomagnetic effects produced from various currents in the magnetosphere and the ionosphere, in terms of frequency variations. In the subsequent years, Falayi et al., (2017) explored the spectral characteristics of GICs using continuous wavelet transform (CWT) during several geomagnetic storms; Adhikari et al. (2017) found a positive correlation between GIC, auroral, and RC activities during geomagnetic storms; Khanal et al. (2019) found that long-duration high-intensity substorm activity drives continuous small-amplitude fluctuation in GIC over several days, the cumulative effect of which is important for pipeline corrosion; Orr et al. (2021) analyzed the network response of GICs in the United Kingdom using wavelet transform and found a correlation to auroral electrojets.

We add to the literature by using the property of scales from wavelet analysis to learn about the underlying frequencies during peak GICs and data fusion of ground and space-based observations, gathered at different resolutions, for physical interpretation of the CWT results. We



adopt the idea of data fusion coined by Hall & Llinas (1997) who defined it as combining data from multiple sensors and related information from associated databases to achieve improved accuracy and more specific inferences than could be achieved using a single sensor alone. This not only helps us overcome the challenge of using datasets from different sources with non-uniform sampling periods but also allows us to analyze them together for an integrated picture. In this paper, we show that wavelet analysis of ground data (GIC and BH) supplemented with systematic fusion of observations and prior modeling, reveals GICs as a natural consequence of multi-scale ionospheric activity driven by magnetosphere dynamics.

## 2 Data and Method

**Ground-based data:** We use the 10-s GIC data measured in the Finnish natural gas pipeline at Mäntsälä (MAN, 60.6N GLAT / 57 MLAT) on 17 March 2013. The corresponding **B** is measured by the reference magnetometer at Nurmijärvi (NUR, 60.5N GLAT / 57 MLAT) 30 km east of MAN (Pulkkinen, Viljanen, et al., 2001; Viljanen et al., 2006). We 10-s resolution International Monitor for Auroral Geomagnetic Effects (IMAGE) magnetometer-derived 2D Equivalent Currents (EC) (Tanskanen, 2009), 1-minute SuperMAG products (Newell & Gjerloev, 2011, 2012; Waters et al., 2015), and 2-minute Super Dual Auroral Radar Network (SuperDARN) products (Greenwald et al., 1995) for assessing the ionospheric activity.

It is important to note that MAN sits at the central junction the pipeline that spans 350 km in the east-west direction and about 120 km in the north-south direction. Although, Pulkkinen, Pirjola, et al. (2001) note that the Finnish pipeline is electrically connected to the Russian pipeline, the GICs induced far in the Russian side of the network does not reach very far to the Finnish side. They also note that although the GIC is measured at a single location (MAN), it is

influenced by activity over the entire pipeline. In contrast, NUR is not a part of an electrically connected network and hence will have slight differences in the signal fluctuations.

**Space-based data:** We use Active Magnetosphere and Planetary Electrodynmic Response Experiment (AMPERE) fitted Field Aligned Current (FAC) data (10-minute averaged) and plots (Anderson et al., 2002; Waters et al., 2001) for assessing the M-I coupling. Energetic Neutral Atom (ENA) 15-minute averaged images from Two Wide-Angle Imaging Neutral-atom Spectrometers (TWINS) instrument provide information about the RC population distribution (McComas et al., 2009). The solar wind observations, Sym-H, and AE indices are from (King & Papitashvili, 2005).

For TWINS images, we performed a sensor-dependent flat-field and background subtraction for each image following McComas et al. (2012) a flat-field image was produced: i.e., any flux mismatch at the boundaries between adjacent TWINS sensor heads was removed by subtracting the excess from the higher-flux side. Then, the minimum measured flux along the outermost edge of the flat-field image field-of-view (FOV) was subtracted from the entire image.

## **Method: Wavelet Analysis + Information fusion**

We analyze the 1-D time-series of GIC at MAN and  $BH = \sqrt{B_X^2 + B_Y^2}$ , at NUR using wavelet analysis techniques. We favor the use of frequency analysis of BH rather than  $dB_X/dt$  in our study to capture all underlying frequencies from all directions, which can be important for scientific investigations (Heyns et al., 2021; Watari et al., 2009).

### **2.1 Continuous Wavelet Transform (CWT)**

Given the continuous nature of the signal, and the relationship of the magnetic field to GIC in the frequency domain, CWT emerges as the optimal tool for analyzing this event.

Importantly, CWT exhibits high resistance to signal noise (Slavič et al., 2003), making it particularly advantageous for the analysis of potentially noisy GIC data (Pulkkinen, Viljanen, et al., 2001). CWT is a convolution of the input data sequence (GIC and BH) with a set of functions generated by the mother wavelet. We employ the ‘Morlet’ mother wavelet, based on its good time-frequency localization capabilities (Grinsted et al., 2004; Khanal et al., 2019; Torrence & Compo, 1998; W.-H. Xu et al., 2022).

CWT coefficients  $C(a,b)$  are calculated using Eq. 1 such that the continuous wavelet function,  $\psi(t)$  is shifted using the position parameter ‘b,’ across the time-series  $x(t)$  with changing scale factor ‘a’ which stretches the wavelet to provide a 2-D representation of time-localized oscillations of a 1-D signal.

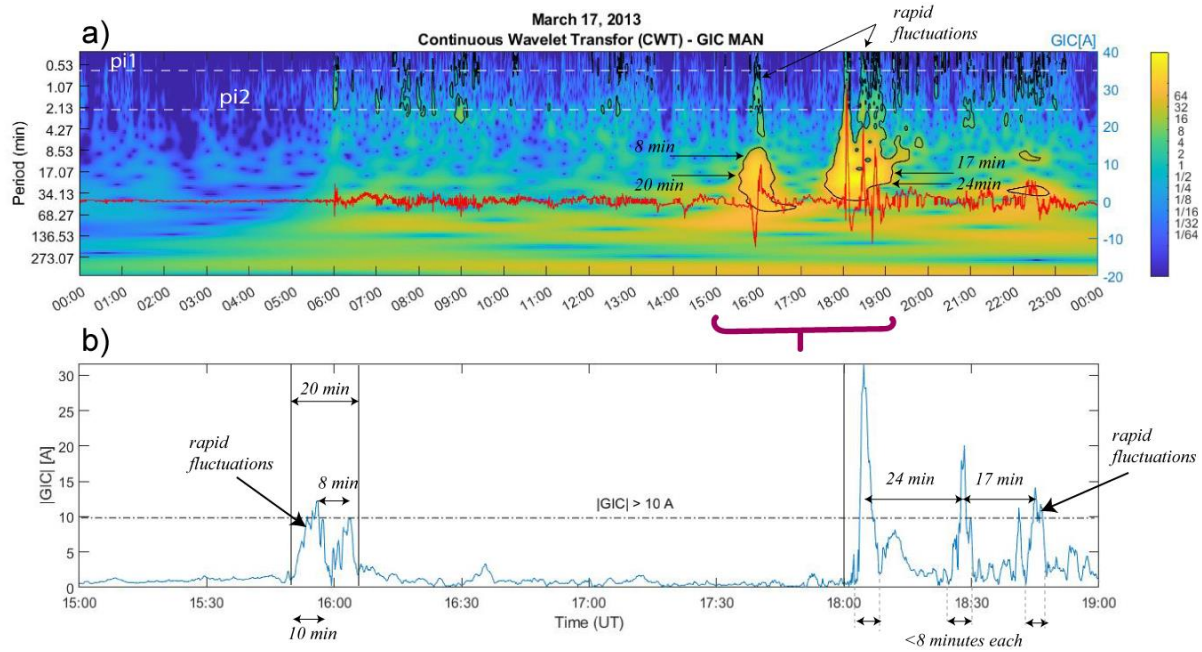
$$C(a, b) = \frac{1}{\sqrt{(a)}} \int_{-\infty}^{\infty} x(t) \psi \left( t - \frac{b}{a} \right) dt \quad \dots\dots\dots (1)$$

The heatmap in Fig. 2a shows the power spectrum of the CWT of GIC, calculated using Eq. 2,

$$\text{Wavelet power Spectrum} = |C(a, b)|^2 \quad \dots\dots\dots (2)$$

To differentiate between underlying periodicities and noise, Torrence & Compo (1998) created a statistical significance test for determining the significance of the time-localized oscillation in the wavelet power spectra. Fig. 2b shows the zoomed version of the GIC amplitude time-series

204 between 15-19 UT to confirm that CWT shows significant identifiable periodicities.



205

206 **Figure 2: a) Continuous Wavelet Transform (CWT) of GIC shown as heatmap overlaid with**  
 207 **GIC time-series. The left axis indicates period [minutes]; the right axis indicates GIC [A].**  
 208 **Yellow indicates high wavelet power. Black contour lines indicate time-frequency oscillations**  
 209 **that are statistically significant (95% confidence). The frequency boundaries for Pi1 and Pi2**  
 210 **pulsation ranges are shown in white. b) GIC time-series (absolute values) zoomed on 15:00-**  
 211 **19:00 UT to show the underlying periodicities. Annotated arrows in a) show key periods**  
 212 **identified in the time-series.**

## 2.2 Cross Wavelet Transform (XWT) and Wavelet Coherence (WTC)

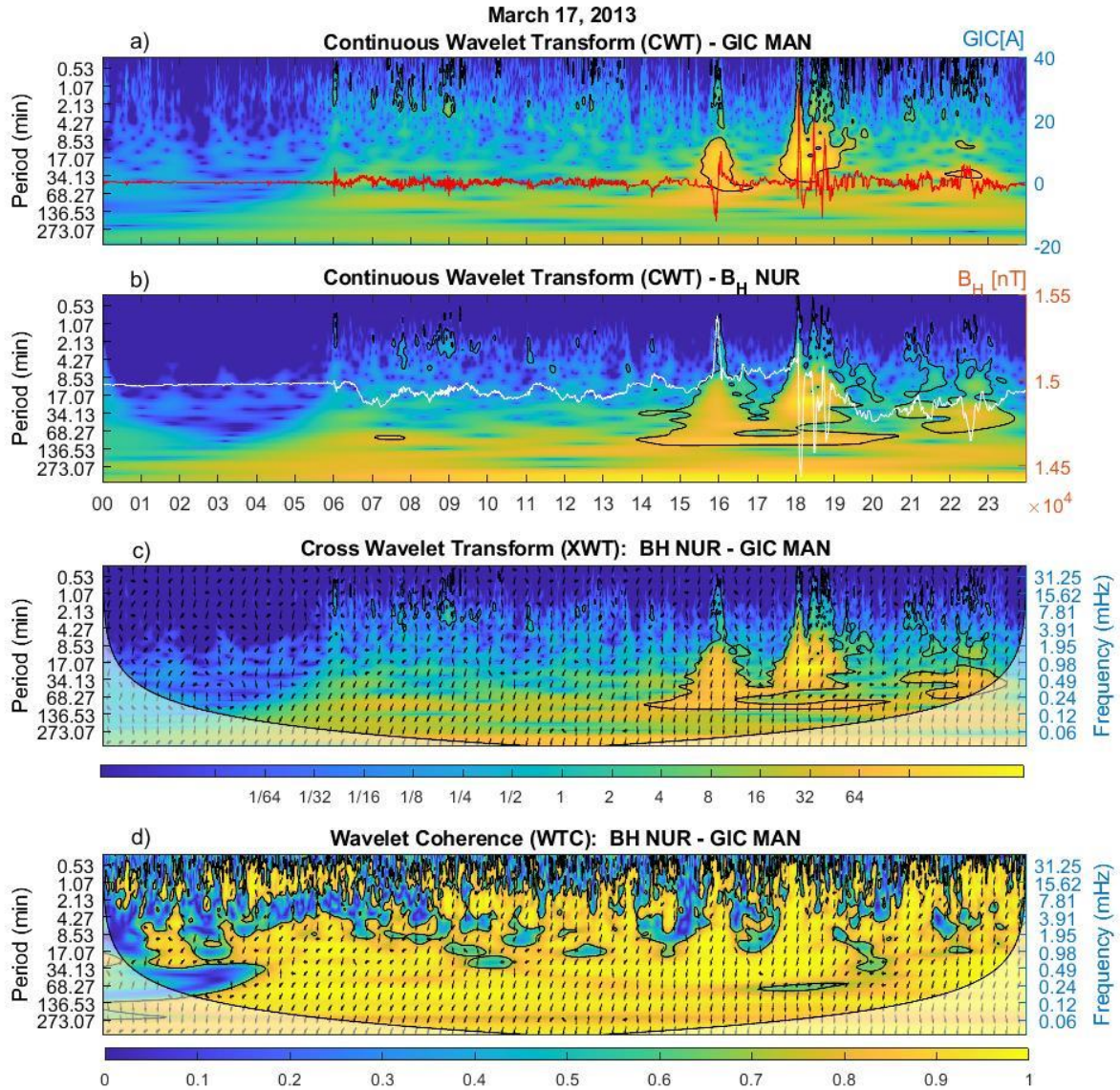


**Figure 3: Wavelet analysis - a) Repeat Fig. 2a. b) CWT of BH at NUR overlaid with BH Time-series [Right axis indicates the magnitude of BH [nT]]; c) Cross Wavelet Spectrum (XWT) of GIC and B-field with phase arrows indicating lag between the time-series; d) Wavelet Coherence of (WTC) of GIC and B-field indicating the correlation between the two time-series. Left Axis indicates period [min]. The black arrows in (c) and (d) indicate the phase angle between the two time-series. Translucent highlights at bottom left and right corners show cone of influence.**

Grinsted et al. (2004) extended the statistical test to cross-wavelet analyses. We adapt their code (<https://grinsted.github.io/wavelet-coherence>) to generate Fig.3. The associated equations for creating the plots have been described in detail by the authors. This method ascertains that the time-frequency oscillations of any signal are significantly different from the background red noise power spectrum (that captures randomness typically found in geophysical time-series) and that the power spectrum of GIC is neither noise nor random. Fig. 3a-b show the CWT of GIC and BH respectively.

The XWT between BH and GIC identifies common time-frequency oscillations and shows the relative lag between the two time-series as small black arrows overlayed on the color map. The phase arrows represent the following: right (in-phase), left (anti-phase), down (BH leading GIC by  $90^\circ$ ), and up (GIC leading BH by  $90^\circ$ ). WTC resembles the traditional correlation coefficient but is superior to that since it shows a correlation between the two signals at different frequencies. Fig. 3c shows the power of XWT coefficients with similar color schemes as CWT. Fig. 3d shows the WTC colormap with yellow indicating a high correlation and blue indicating a low correlation.

The CWT, XWT, and WTC have edge artifacts because the wavelet is not completely localized in time. It is therefore useful to introduce a Cone of Influence (COI) in which edge effects cannot be ignored, which is shown as gray highlighted region in the bottom right and bottom left corners of the plots. The COI is removed from panels d and e to show the time-series clearly (GIC and BH respectively), but it occupies the same area as (c) and (d).



### 2.3 Ground-Up Approach to Information Fusion

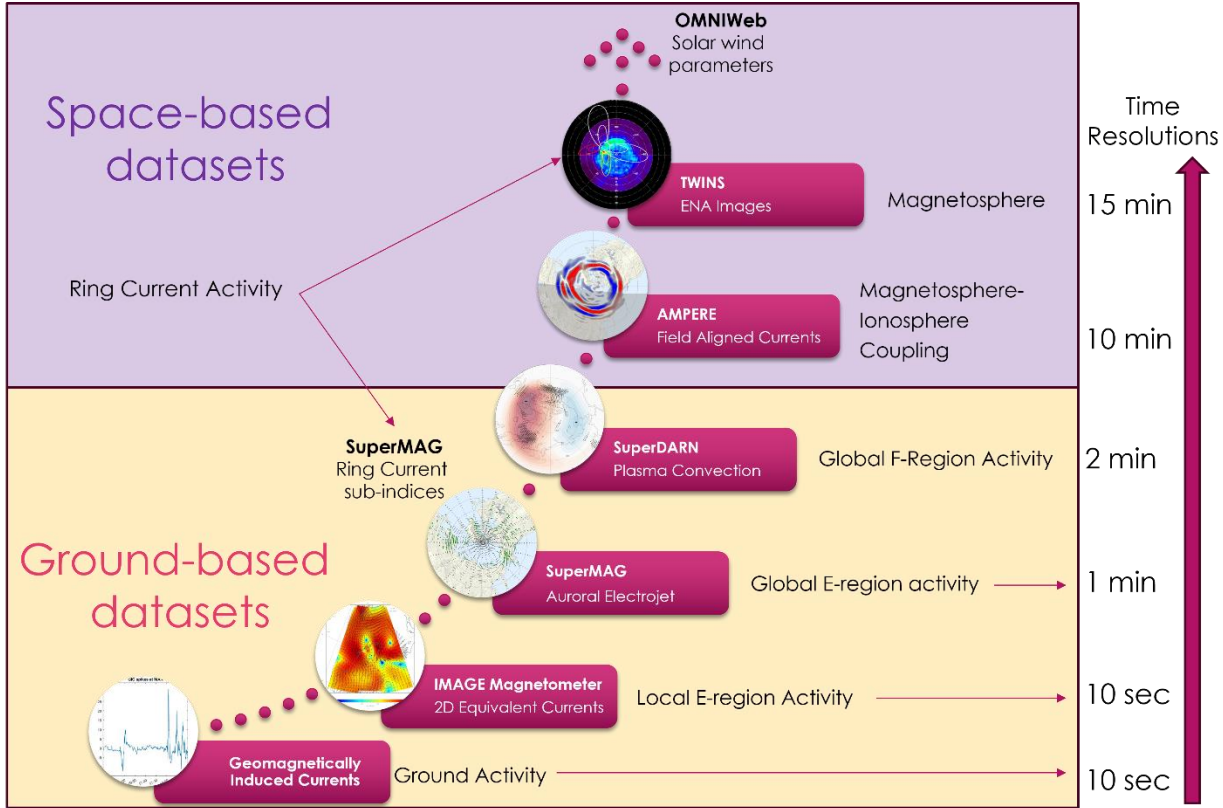


**Figure 4: Summary of datasets used for the Ground-Up Approach using ground and space-based observations. Right side shows the time resolutions of the observations.**

Fig. 4 illustrates the ground-up approach with datasets that sample the activity at different resolutions and altitudes, thus providing support for physical interpretation of the significant multiscale periodicities identified in wavelet plots. We use three tools in this paper – wavelet analysis for time-frequency perspective, global maps for spatial perspective, and keograms for localized-temporal perspective. The waveform (1-D time-series) and wavelet transform (2-D time-frequency heatmaps) reveal underlying frequencies in the GIC and BH signal. Spatial maps around the time of GIC spikes provide a local/global context of ionospheric and magnetospheric activity. Keograms for the evolution of AMPERE-derived FAC and IMAGE 2D-EC provide insights into the magnetospheric drivers and their duration.

### 3 Results

The first GIC spike has a sinusoidal waveform with 12 A peak at 15:56 UT (G1a) and 9.8A peak at 16:04 UT (G1b). For reasons described later, we refer to this as a ‘compound’ GIC. The largest GIC peak of 31.65 A occurs at 18:04 UT (G2). Two more GICs >10 A occur at 18:28 (G3) and 18:46 UT (G4). We discuss the observational differences between these spikes in the rest of the section.

#### 3.1 Spectral Similarities and Differences in Wavelet Analysis

The CWT heatmaps in Figs. 2a and 3a-b show minimal fluctuations in the GIC and BH spectra before the shock arrival at 06 UT; thereafter intensified high-frequency variations are present during the passage of the pre-CME sheath (06 UT - 10 UT) while the MAN/NUR region is on the dayside. The large amplitude GIC spikes occur in tandem with spikes in BH after the magnetic cloud arrives at ~15:30 UT. Both heatmaps show two distinct multi-minute regions of time-frequency oscillations - one at ~16 UT (<1 min to ~30 min period, and the other between 18-19 UT (<1 min to ~1h period). XWT power in Fig. 3c shows phase arrows (down and/or down-left) within the 95% significance contour indicating that BH leads (down) the GIC response and is out-of-phase (left) after 15 UT. This is consistent with W.-H. Xu et al.'s (2022) results and confirms the physical intuition of BH variations driving GICs. The WTC plot (Fig. 3d) shows a low correlation in the two time-series at higher frequencies before the shock arrival and a high correlation thereafter. The correlation is much higher across all frequencies during GIC spikes. That is: the duration and variation of activity affecting BH is also reflected in the GIC signal.

The key takeaway from the spectral analysis is that around 16 UT, the ‘compound’ GIC spikes occur over 20 minutes with peaks having an 8-minute separation. Subsequently, three



periodic spikes (G2-G4) occur over 40 minutes; G2 and G3 are 24 minutes apart and G3 and G4 are 17 minutes apart. The higher frequency fluctuations in the range Pi1 and Pi2 (periods < 40 s and 40-150 s, respectively) shown in Fig. 2a have been associated with substorm onset (Saito, 1969 and references therein) which is discussed in Section 4. We suspect there is more Pi2 fluctuation in the GIC signal compared to BH (or dBx/dt from W.-H. Xu et al. (2022)) due to the integrated effect over the pipeline.

### 3.2 Ionospheric Activity and Coupling with Magnetosphere

The combination of signal waveform and spectral heatmap suggests different driver(s) for the GIC spike around 16 UT compared to spikes between 18-19 UT. We explore the ionospheric activity and the associated coupling with the magnetosphere to learn about the different drivers in Fig. 5. The first column shows the local IMAGE 2D-EC spatial map over Finland while the second column shows the global map of the SuperMAG equivalent currents in the northern hemisphere. The third and fourth columns show polar plots of the NH SuperDARN convection maps and AMPERE FACs, respectively. We organize the spatial maps in increasing altitudes and temporal resolutions, which also capture multiscale M-I activities.

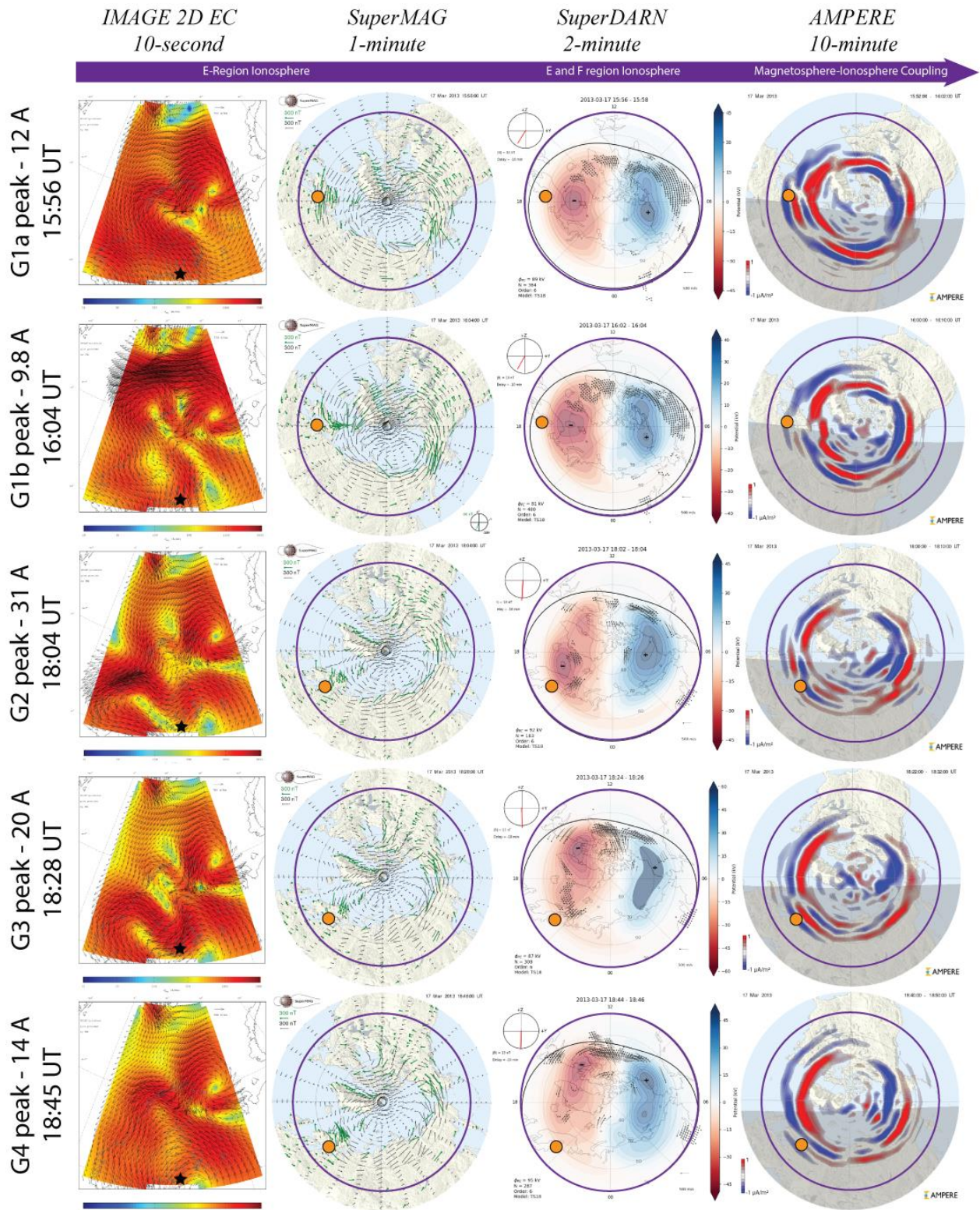


**Figure 5: Matrix of observations (Top to Bottom) Ionospheric activity and coupling with magnetosphere during the instances of peak GICs labeled as G1a, G1b, G2, G3, G4. (Left to**

*right) IMAGE 2D Equivalent Currents (EC) [NUR marked with black star], SuperMAG plots with green vectors indicating electrojet pattern, SuperDARN convection maps with black vectors showing plasma velocity. AMPERE-derived upward (red) and downward (blue) FACs, Outlines mark 50 MLAT on all plots. Location of MAN marked as orange circle.*

The interval at ~16 UT, shows two GIC extrema occurring within 20-minutes. The top row of Fig. 5 shows NUR station (black star) at 15:56 UT under a region of strong equivalent current at the equatorward edge of the IMAGE 2D-EC map. SuperMAG suggests a strong localized eastward electrojet (eEJ) over MAN/NUR, with a broad westward auroral electrojet (wEJ) poleward of the location. This is consistent with the rising trend in BH. Although the SuperDARN convection map lacks duskside plasma velocity vectors, possibly due to the expanded auroral oval, the line-of-sight (LoS) spectrogram of plasma velocity (see supporting information Fig. S1) shows near-range echoes at Hankasalmi station, indicating activity in the E-region and suggestive of an enhanced eEJ. AMPERE-derived FACs show a highly structured layered pattern (alternating reds and blues) from the pole to the equator, with MAN/NUR beneath the transition of upward and downward FACs. For context, typically, Region 1 (R1) FAC points into the ionosphere on the dawnside (blue) and out of the ionosphere on the duskside (red) whereas Region 2 (R2) FAC (equatorward of R1) points downward on the duskside and upward on the dawn-side (Iijima & Potemra, 1976). The DMSP SSUSI emission maps (see Fig. S2) show duskside precipitation stretching from 65°-75° MLAT, indicative of highly structured ionospheric conductivity.

The second row of Fig. 5 follows the same sequence for 16:04 UT. The IMAGE 2D-EC gained a significantly structured north-south component. Similarly, the SuperMAG plot reveals a narrow equivalent-current channel north of MAN. The AMPERE-derived FACs show that the layered structure has subsided and the R1 FAC at 18 MLT has moved poleward. The DMSP

Southern Hemisphere emission map (Fig. S2) shows a bright spot just above 65° MLAT and slightly west of the 18 MLT line.

The bottom three rows in Fig. 5 suggest that MAN/NUR were under the influence of shearing eastward and westward electrojets during G2-G4. The SuperDARN convection maps show that a mesoscale plasma vortex structure (identified by the tight curl) forms and dissipates over the three timestamps. FACs appear to have a complex upward and downward structure. The sequence of observations shown in Fig. 5 suggests different magnetospheric mechanisms affecting the ionosphere at G1(a and b) compared to G2-G4. We discuss these in Section 4.



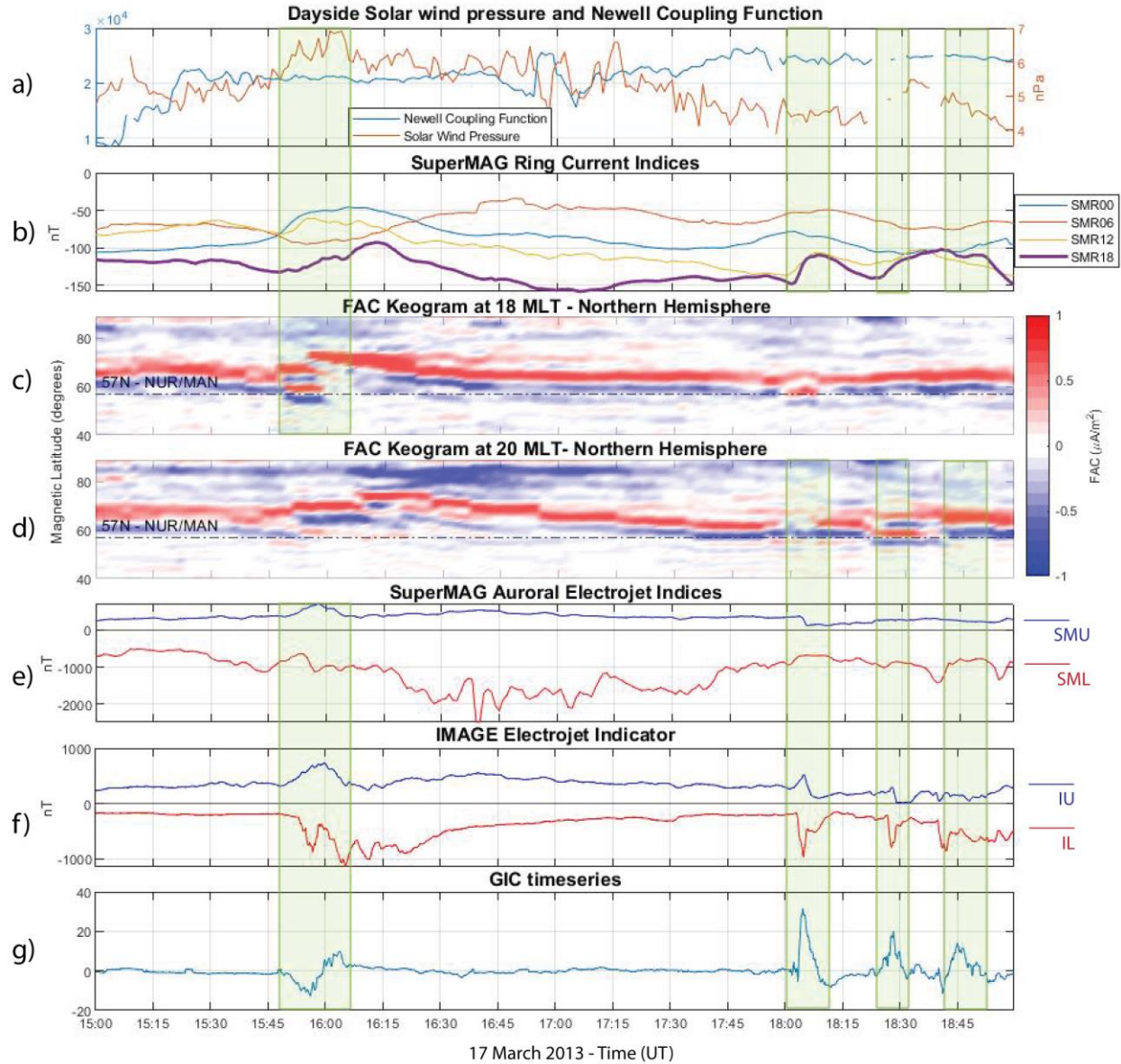


**Figure 6: Ground-to-Space dynamics between 15-19 UT. a) SuperMAG-derived parameters Newell Coupling Function and solar wind dynamic pressure; b) SuperMAG Ring current indices at four local times; c,d) FAC keogram at 18 MLT and 20 MLT respectively. Red indicates upward FAC, Blue indicates downward FAC. e) SuperMAG Auroral Electrojet Index Upper (SMU/eastward) and Lower (SML/westward) values for global substorm activity; f) IMAGE Magnetometer-derived Electrojet Indicator Upper (IU) and Lower (IL) values for local substorm activity; g) GIC signal. Green highlights mark the duration of GIC spikes.**

Additional parameters that add insight to the state of magnetosphere during these GIC spikes are shown in Fig. 6. The rate of magnetic flux addition (Fig. 6a) quantified by the Newell coupling function (Newell et al., 2007) increases from  $1 \times 10^4$  Wb/s to  $2 \times 10^4$  Wb/s from 15:00 to

15:30 UT. Such a flux increase, followed by the rising solar wind pressure (brown curve), should eventually trigger magnetic reconnection on the night side and consequent enhancement of the duskside RC. Figure 6b shows the sector-wise RC proxies. We focus on the SMR18 sub-index since MAN is at dusk. A decrease in the duskside RC intensity around 16 UT is followed by RC intensification for 2 hours before reducing again. In Fig. 6c and d, we show FAC keograms at 18 MLT and 20 MLT, respectively, to focus on the localized coupling during the G1a-b and subsequent spikes. These FACs drive the ionospheric currents (electrojets) and affect the global substorm values (Fig. 6e) of the Auroral Electrojet, which is represented by the SuperMAG SML and SMU indices. These indices are associated with global westward and eastward electrojet activity respectively. The local substorm indices IL and IU derived from IMAGE magnetometer (Fig. 6f) show different features than the global indices suggesting localized effects over the pipeline (Fig. 6g).

The negative GIC peaking at 15:56 UT (G1a) corresponds to 1) intensification of local eEJ (SMU and IU) and dip in local wEJ (IL), 2) downward (blue) FAC split by upward FAC, and c) decreasing RC intensity at midnight, dusk, and noon. The positive GIC peaking 8 minutes later at 16:04 UT (G1b) corresponds to 1) decaying local eEJ with a second dip in IL, and 2) poleward movement of R1 FAC with weakened equatorward layers. This suggests a major reconfiguration in the regional M-I coupling. During G2-G4, there is a decrease in global auroral indices, complex FAC structure, and fluctuating RC intensity at dusk but an increase in intensity at midnight. These spikes rise and fall thrice over a duration of 40 minutes, again, captured by CWT as significant periods (Fig. 2). From Fig. 6, we infer that the G2-G4 spikes are a result of localized M-I coupling.

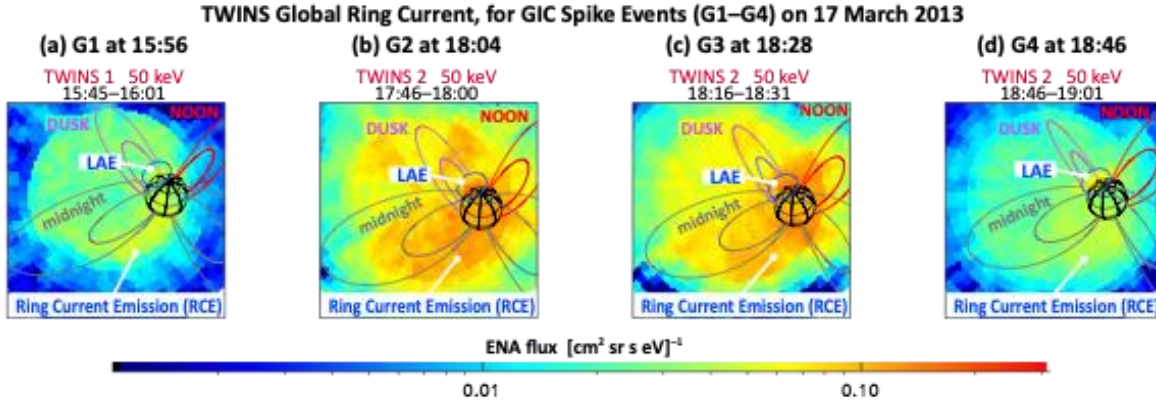


**Figure 7: TWINS ENA images of 50keV particles showing large-scale ring current (RC) activity when GIC spikes (G1 – G4) are recorded. In each image, the Earth is depicted, and dipole field lines are drawn at L=4 and 8 (Red = noon MLT, purple = dusk MLT). Each  $4^\circ \times 4^\circ$  ENA image is integrated over 15 minutes. Each image includes a ring current emission (RCE) and low altitude emissions (LAE).**

The TWINS ENA images provide a large-scale perspective of the inner magnetospheric state and RC dynamics. Figure 7 shows snapshots of 50 keV ENA images, at the nearest available times to the four GIC spikes. Each image contains the following information – Earth’s, the two dipole field lines at L=4 and 8 with color coding to indicate MLT: red (noon), purple (dusk), and grey (midnight and dawn). Each pixel indicates line-of-sight (LOS) integrated ENA flux, accumulated over 15 min. On 17 March 2013, both TWINS 1 and 2 imagers frequently observed elevated background counts, most likely from local (to TWINS) energetic ions penetrating past the collimator plates that are supposed to keep these ambient ions out (McComas et al., 2012). Hence, we performed a sensor-dependent flat-field and background subtraction for each TWINS image described in the Data and Method section.

During all GIC spikes, the presence of Low Altitude emission (LAE) suggests significant ion precipitation from the duskside RC, even though the ENA flux appears weaker there. The reason could be anisotropic duskside ion pitch angle distributions (PADs) generating fewer ENAs in the directions of the TWINS locations (Goldstein et al., 2012), rather than from a

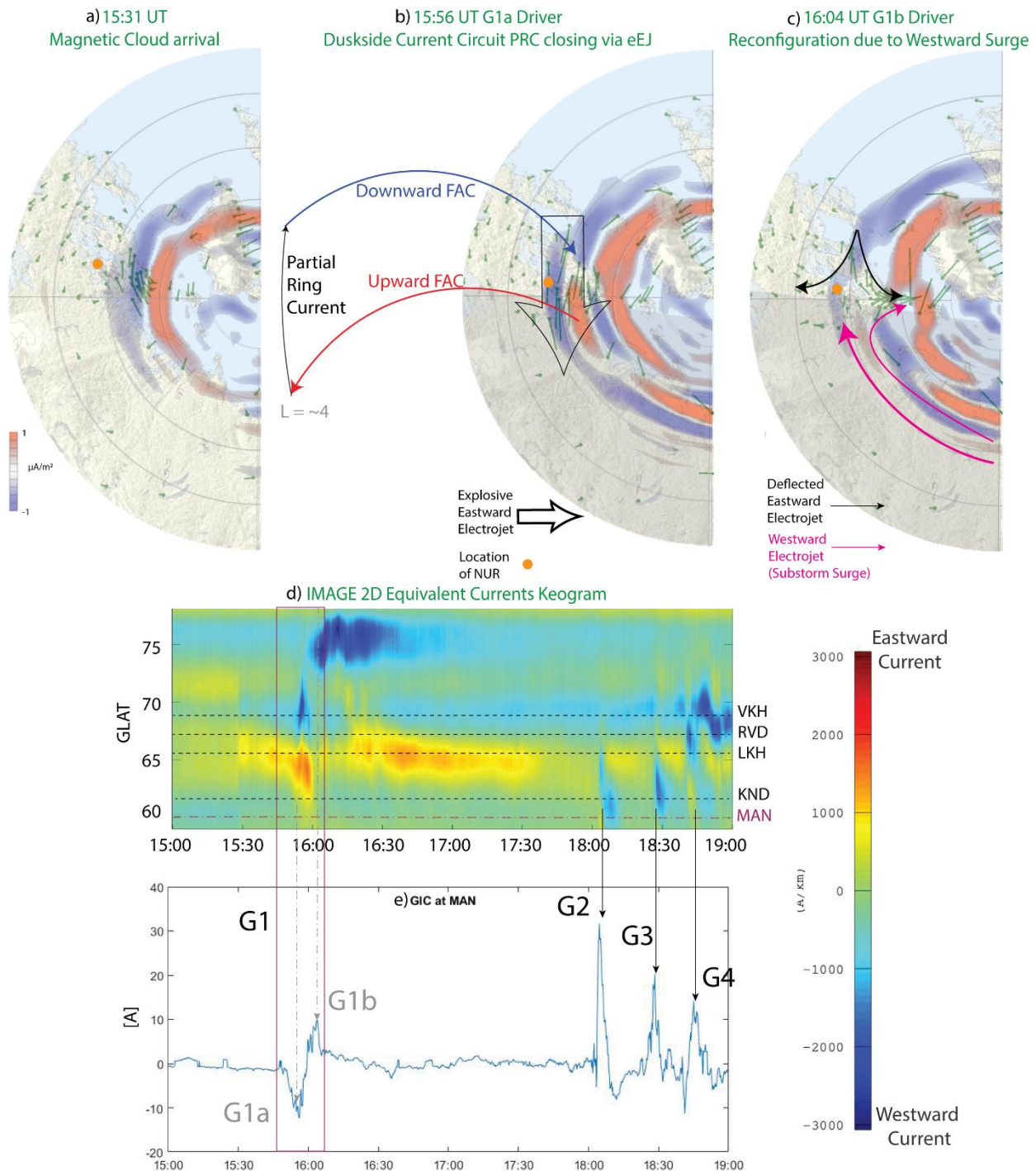
weaker RC. Near the time of G1a (Fig. 7a), TWINS observed a weak RCE and modest LAE at dusk. This LAE enhancement was not observed in the image 15 minutes before, indicating new RC activity enhanced the precipitation. Near the times of the larger GIC spikes of G2–G4, TWINS imaged a significant global RC enhancement, as well as an LAE intensification. For the largest GIC peak, G2, the RCE was enhanced most strongly in the post-midnight sector, but also in patches of enhanced ENA flux near dusk (Fig. 7b). The non-uniformity of the duskside increase may reflect an MLT-dependent PAD evolution that modulates the ENA intensity, but also may be (at least partly) an artifact from the background subtraction. The closest-in-time images to G3 (Fig. 7c) and G4 (Fig. 7d) likewise depict global RC changes concomitant to the strength of the GICs. That is, these TWINS imaging observations confirm the difference in RC activity corresponding to the GIC spikes, indicating magnetospheric sources for the GICs. Søråas et al. (2018) provide strong supporting evidence based on NOAA and MetOps satellite particle precipitation data. They note that the isotropic particle precipitation (PP) in the upper atmosphere is related to particles injected from plasmasheet (BBF) into the inner magnetosphere (up to  $L = 2.7$ ) and hence is a proxy for RC injections. They further find an increase in ENA flux around 15-19 UT in the equatorial region and elevated PP in the RC energy range over MAN (50-60 MLAT). Hence, the duskside LAE signal in Fig. 7 can be explained by precipitation originating from RC injections.

#### **4. Discussion**

We consider impinging mesoscale plasma flows as likely GIC sources. Based on available data and models, we argue that the magnetospheric source(s) of the compound GIC spikes at 16 UT was a larger and more energetic flow burst than those driving the self-similar GIC spikes between 18-19 UT.



## 405 4.1 Drivers of GIC peak at ~16 UT



406  
407 **Figure 8 a-c): AMPERE-derived FACs superposed on SuperMAG plot with 50% transparency**  
408 **at 15:56 UT (G1a) and 16:04 (G1b) to interpret their drivers. Arrows indicate the direction of**  
409 **eastward and westward ionospheric current surges d) IMAGE 2D-EC keogram with 15 to 19**  
410 **UT. MAN latitude marked in red dotted line. Transformer stations (VKH, KND, RVD, LKH) in**  
411 **the Kola Peninsula (Belakhovsky et al. 2019) marked in dotted black lines, e) Repeat of Fig 6g.**

*G1 highlighted in the box. Arrows show the connection between overhead ionospheric activity driving GICs.*

For context, Fig. 8 (top row) shows polar views of the near-dusk equivalent current system with AMPERE FACs overlayed. Figure 8a displays the current pattern as the magnetic cloud passed Earth when the duskside was dominated by an Ijima-Potemra FAC pattern, typical of a well-developed RC. The negative portion of G1 (Figs. 8b and e) coincided with a major current reconfiguration and a sudden duskside eEJ enhancement. The positive portion of G1 (Figs. 8c and e) coincided with another major current reconfiguration and a sudden development of a poleward equivalent current channel and an enhanced wEJ at high latitudes. Recall also that the CWT (Figs. 2 and 3a-b) showed distinct Pi1/Pi2 pulsations during the 30-minute interval around 16 UT, which are indicative of substorm activity in the auroral and subauroral regions (Kepko & Kivelson, 1999; Milling et al., 2008 and references therein).

**Event G1a.** Figure 8b (15:56 UT, G1a) shows the most intense eEJ developed near 60° MLAT close to the southern end of the pipeline. The nearby NUR magnetometer recorded a positive deviation in BH lasting for ~30 min (Figs. 1b and 3b), consistent with the rising IL index in Fig. 6f. With the already strong RC (Fig. 6b), the *prima facie* evidence is that the G1a spike was driven by a sudden PRC closure (see the current loop in Fig. 8b) that increased eastward current in the duskside ionosphere. Supporting this is the sudden TWINS LAE (Fig. 7a) and conjugate DMSP F16 and F17 particle data for the SH (not shown) that confirm new RC precipitation (10-40 keV ions) equatorward of -60° MLAT. Below we build a case that supports G1a and G1b activity as driven by an impinging mesoscale flow channel that influenced current systems across a range of latitudes.

Kamide & Fukushima (1972) championed the idea of a PRC closing via an eEJ in the duskside ionosphere as part of long-lived, storm-time-enhanced convection event. In contrast, the pre-16 UT eEJ enhancement was short-lived and seemingly disrupted by a major duskside current reconfiguration within 10 minutes. Grafe et al. (1998) and Feldstein et al. (1999) designated similar transient, duskside eEJs as ‘explosive’ events and noted an association with substorm-driven wEJ onset at higher latitudes, although the exact timing and relationship between the electrojets was unclear. Chen et al. (2020) reported that strong substorm injections generate Electromagnetic Ion Cyclotron (EMIC) waves in the dusk sector. This leads to an inference that wide flow channel penetrated the duskside inner magnetosphere and created waves that triggered RC precipitation at the duskside plasmopause bulge/plume as suggested by Trakhtengerts & Demekhov (2005) and Spasojevic & Fuselier (2009) thus, potentially contributing to the formation of a PRC-driven eEJ at  $L \leq 5$ . A superposed epoch analysis by D’Onofrio et al. (2014) showed that eEJ enhancement precedes wEJ enhancement during moderate substorms.

Using EISCAT and IMAGE magnetic observatories and several Russian observatories, as well as DMSP particle data, Feldstein et al. (1999) determined that the equatorward side of eEJ was bounded by the plasmopause projection to ionospheric height, and that the poleward boundary of eEJ was the ionospheric projection of the plasmasheet inner boundary. During substorms the wEJ widened to fill the auroral zone and at times forced the auroral boundary poleward. They reasoned that the storm time eEJ in the evening sector of the magnetosphere linked to processes in the inner magnetospheric regions adjacent to the plasmasheet inner boundary.

Feldstein et al. (2006) studied the 25 September 1998 storm and found that eEJ had contributions from a PRC closure at lower latitudes as part of an intense substorm-sub auroral polarization stream (SAPS) interaction. Yang et al. (2012) simulated a strong plasma bubble injection impinging on the nightside ionosphere (23 MLT). One obvious effect in the simulation was the creation of a SCW two-loop (SCW2L) circuit of evolving R1 and R2 currents that match the pattern evolution shown in Figs. 8b and 8c. Mishin et al. (2017), studying both the 25 September 1998 event and the 17 March 2013 event, established a causal relationship between fast RC injection via mesoscale flow channels, a SCW (westward moving front creating Pi2 pulsations), and duskside SAPS via an SCW2L.

Prior studies of the 17 March 2013 event reveal that: 1) near dusk, the plasmasphere was eroded to  $< 4 R_E$  (Krall et al., 2017) leading to Pc1 fluctuations and injection signatures in the Russian ( $50^\circ$ - $60^\circ$  GLAT) sector (Potapov et al., 2017); 2) the RC was well-developed and supported an active SAPS channel near  $L = 4$  (Ferdousi et al., 2019; Lin et al., 2021); and 3) Sorathia et al. (2018)'s simulation shows a wide plasma injection (mesoscale flow channel) in the evening sector, although the modeled injection impinged slightly later in MLT. Thus, Figs. 8a-d along with results in Section 3 support the idea of 'compound' 16 UT GIC with negative-then-positive spikes (Fig. 8d) driven by a dusk-region bubble injection/substorm. The injection first disturbed the RC and then the auroral zone. While we have insufficient information to determine how the large-scale current systems were being modified by mesoscale drivers to produce the GICs, we anticipate that additional coupled mesoscale simulations (e.g. Bao et al., 2023) could provide insight into the related physics.

**Event G1b.** Just before 16 UT significant global and local changes in the geomagnetic field occurred. The equivalent current and FAC patterns shown in Figs. 8a and 8b were

disrupted. We associate these changes with event G1b. Over Finland and Kola regions, meridional equivalent currents rapidly replaced the east-west currents. From 15:56 to 16:04 UT on the Mäntsälä pipeline, the minimum-to-peak GIC variation was 22 A; in the same interval, there was a 70 A variation at Vykhodnoi power station in the Kola Peninsula. Figure 8c displays the currents for 16:04 UT (G1b) and shows an intense poleward current channel over the north end of the pipeline and the Kola peninsula, where strong ground magnetic fluctuations were observed (Belakhovsky et al., 2019; Despirak et al., 2022). The narrow current channel, bracketed by up-down FACs (Fig. 8c) and a poleward displacement of the R1-FAC (Figs. 6d) are consistent with the description of auroral streamer development during arrival of plasma flow bursts (e.g. Hubert et al., 2007; Zou et al., 2022). It was also during this time that significant Pi2 fluctuations appeared in the MAN CWT (Fig. 2a). Although we lack auroral imagery during this time frame, we offer streamer development near the north end of the pipelines as a plausible cause of G1b. The sharp enhancement in POES/MetOps particle precipitation data supports this idea (see Figure S3),

Two essential findings arise from this synthesis: 1) based on observational evidence, we assert that afternoon eEJ, perhaps amplified by substorm dynamics, can lead to significant GIC spikes near dusk and 2) based on circumstantial evidence we assert that the meridional equivalent current channel and related FACs are a further (substorm) manifestation of the energetic mesoscale plasma flow and a source of GICs. In the next section, we address a set of related GIC spikes that may be more typical of the storm recovery phase.

## **4.2 Driver of GIC peaks between 18-19 UT**

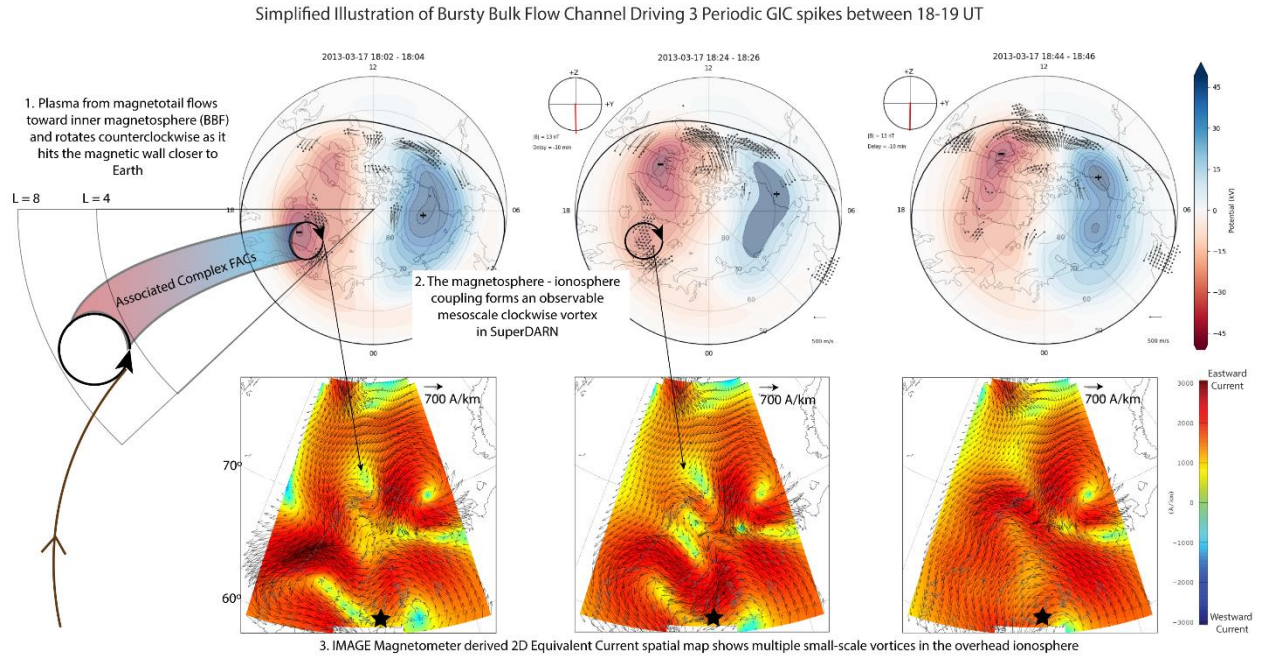


**Figure 9: Illustration of BBF creating three meso-scale vortices (SuperDARN) in the topside ionosphere leading to smaller-scale vortices (IMAGE 2D-EC) that eventually lead to the three periodic GIC spikes.**

Approximately two hours after G1, three periodic spikes arise when MAN is in the post dusk region ( $\sim 20$  MLT). In Fig. 5, the SuperMAG plots show MAN situated under opposing eastward and westward current vectors. Movie S1 clarifies that the vectors rotate counterclockwise as localized mesoscale vortices three times. The direction of the vortices is consistent with the SuperDARN clockwise vortex-like structure. These vortices occur simultaneously with local electrojet index spikes (Fig. 6f) and GICs. In the SuperDARN convection map, a meso-scale vortex is located between  $\sim 65$ - $70$  MLAT and  $18$ - $21$  MLT (poleward of MAN). Using  $L = \frac{r}{\cos^2(\lambda)}$  where  $\lambda$  is the geomagnetic latitude and  $r = 1\text{Re}$ , the  $60$ - $70$  MLAT in the ionosphere traces into the equatorial magnetosphere at a distance of  $\sim 4$  to  $8$  Re in the post-dusk region. In this region Sorathia et al. (2018, 2023)'s MHD simulation movies show increased bursty bulk flow (BBFs) between  $18$ - $19$  UT.

Figure 9 illustrates the idea of BBFs driving GICs, as suggested by Wei et al. (2021) who reported that BBF-associated FACs alter ionospheric currents and create  $dB/dt$  variations. Keiling et al. (2009) note vortices in equivalent ionospheric currents could be related to magnetospheric plasma flows. BBFs are rapidly flowing plasma channels from magnetotail to the inner magnetosphere. As BBFs approach closer to Earth, the flow speed reduces and eventually hits ‘a magnetic wall’. This causes the plasma to rotate away from Earth to form a vortex-like structure and merge into the RC (Yu et al. (2017) and references therein). We observe clockwise (cw) plasma vortex in the SuperDARN (Fig 9 top row) convection maps. Based on M-I coupling, we can infer that the cw-rotation in SuperDARN convection map is due to a counterclockwise plasma rotation in the equatorial magnetosphere. Velocity direction ( $\mathbf{v}$ ) is governed by  $\mathbf{v} = \mathbf{E} \times \mathbf{B}$ , where  $\mathbf{v}$  rotates clockwise and  $\mathbf{B}$  points toward the earth’s surface in the high-latitude ionosphere, which results in  $\mathbf{E}$  directed toward the center of the vortex. Assuming equipotential lines, the ionospheric  $\mathbf{E}$  has the same direction in the equatorial magnetosphere, but  $\mathbf{B}$  is parallel to the earth’s surface at the equator, thus the plasma circulation is counterclockwise. The 10-minute FAC maps in Fig. 5 (rows 3-5) shows a layered structure making it difficult to decipher the exact dynamics, but the simulation by Sorathia et al. (2023) shows the complex evolution of BBF-associated FACs in the 20 MLT sector, where we note the vortices. To summarize Fig. 9, the BBFs in the post-dusk magnetosphere create meso-scale vortices in the ionosphere inferred from SuperDARN (and SuperMAG) via FACs, that likely result in rapidly changing small-scale vortices observed in IMAGE 2D-ECs, forming three periodic GIC spikes.

Juusola et al. (2009) studied the ionospheric signature of BBF using the IMAGE 2D-EC maps and Cluster satellite-data. They found that the average duration of BBF was 8 minutes (also seen in Fig. 2b) accompanied by a northwest channel at high latitudes (62-76 MLAT) creating a

pair of small-scale upward and downward FACs. Recently, Engebretson et al. (2024) found that BBF drive short-lived high amplitude  $dB/dt$  spikes (like 17 March 2013) using the Canadian ground-magnetometers and THEMIS satellite-data in the 23-01 MLT sector, consistent with Juusola et al's (2009) findings. They estimate that a flow channel, during quiet conditions, creates an oval of  $\sim 180$  km (east-west) by 90 km (north-south) in the ionosphere, which is an order of magnitude smaller than the vortex we note in Fig 9. We suspect that the signature reported by these authors can be amplified in moderate storm by creating either wider flow channels or the mesoscale vortices are superposed on smaller-scale vortices, which would be consistent with the multi-minute spectral area in CWT.

The dearth of duskside in-situ satellite observations on 17 March 2013 the BBF interpretation an inference, but the presence of Pi1/Pi2 pulsations and the  $<8$ -minute duration of spikes (Fig. 2a) provide confidence. First, these substorm-associated pulsations are present in BH and GIC heatmaps (Figs. 3a-b) when the local westward (substorm) currents are enhanced (Fig. 6f). These BBFs produce small-scale wedgelets that combine to form a large-scale SCW (Palin et al., 2016) while also enhancing the RC (Fig. 7b-d) (Goldstein et al., 2020; Sciola et al., 2023). The flows that penetrate the inner magnetosphere create a compression, which has been observed to create oscillations of 1-2 minutes periodicity on the ground (Kepko et al., 2001; Lysak et al., 2015), like Pi2 pulsations in Figs 3a-b. Hence, the observations presented herein, supported by previous studies, suggest that BBFs generate magnetospheric vortices, which connect to the ionosphere by FACs, whose ionospheric closure can cause GICs. Our work extends the relationship from BBF driving short-lived large amplitude GMD directly to GICs.

Belakhovsky et al. (2019) reported substorm-associated ionospheric vortices over the Kola Peninsula between 15-19 UT. (See Fig. 8d for latitudes of the transformer stations



discussed in Fig. 7 of their paper.) Simultaneously, the low-latitude Wp index (Nosé et al., 2012) showed elevated substorm (Pi2) activity. Low-latitude Pi2s are now known to be associated with FACs produced by BBF braking (Cao et al., 2008). Importantly, Figure 7a of Z. Xu et al. (2017) provides a global context of the mid-to-low latitude Bx dynamics wherein we find the fingerprint of the 4 mesoscale channels in the dusk sector from 16-18 UT. We contend that the high-latitude vortices, low-latitude substorm indicators, and the sub-auroral G1-G4 disturbance in the Mäntsälä pipeline were latitude-spanning effects of a series of mesoscale flow injections or impingements. Minor timing differences can be attributed to the difference in overhead currents, ground and material conductivity, system configurations, and the north-south orientation of the powerline (Despirak et al., 2022).

We gather the following key insights from this case study. After the magnetic cloud arrived at 15:30 UT, the strong, steady negative Bz initiated a new cycle of magnetotail reconnection. The interaction between duskside substorm-associated plasma bubble injection, RC, and plasmasphere likely created a transient current circuit closing the PRC via mid-latitude eEJ driving G1a. Immediate duskside current reconfiguration produced G1b. As the storm progressed from late main- to recovery-phase and the pipeline moved from dusk toward midnight, small/mesoscale earthward plasma flow (BBFs) took over to form vortices in the mid-latitude ionosphere to create three large spikes. We conclude the discussion by offering a novel perspective - during this event (and perhaps other events), the pipeline (long conducting material) acted as a huge antenna, capturing multi-scale ionospheric activities.

## 5. Contributions and Future Work

Our work addresses the RC-GIC association gap identified by Ganushkina et al. (2017). We suggest storm-time RC dynamics and the mesoscale flows the impinge poleward of the duskside RC play a crucial role in creating sub-auroral GICs. Furthermore, Yu et al. (2022) identified a modeling gap for integrating different spatial and temporal scales to achieve a comprehensive understanding of the entire system. Our approach can provide observational support to such modeling efforts.

Clearly, more work lies ahead. A follow-on wavelet analysis on the IMAGE magnetometer chain, especially on all three components, during this event would provide more insight into the sequence of driving current systems. Also, extending our analysis to conjugate magnetometer (not shown, MAW – -70.67 MLAT) in SH, which shows larger perturbation than NUR around 16 UT, would further illuminate the M-I coupling aspects of hemispheric asymmetry. Analyzing other GIC events similarly will answer a crucial question: Under what circumstances are GICs generated locally (such as 17 March 2013), vs globally (such as the October 2003 Halloween event (Swedish Transformers – (Pulkkinen et al., 2005); New Zealand transformers - (Marshall et al., 2012, 2017); South African Transformers - (Bernhardi et al., 2008)) in addition to MAN)? What causes them to be short- vs long-lived? A co-occurrence study, extending our approach to multiple locations, for a particular event can be useful for assessing the state of the magnetosphere during GIC spikes that arise globally during later events from Solar Cycle 24 onwards when more ground and space-based observations are available. Moreover, a concerted effort between the simulations and our ground-up approach can provide a better understanding of the topic, important for accurate GIC prediction.

604 Ground-based data played a pivotal role in our paper and hence we highlight the need for  
605 a continuous ground-based stream of data. Our extent of interpretation is limited by the 10-  
606 second data which provides substorm onset related information. However, Potapov et al.  
607 (2017)'s frequency analysis of higher cadence magnetometer data (0.2 to 5 /sec) enabled them to  
608 identify a relationship of Pc1 waves with plasmopause dynamics. This underscores the need for  
609 higher sampling frequency data, which not only appears to keep relative peak errors below 10%  
610 for predicting GICs (Grawe & Makela, 2021), but also appears to make the strongest  
611 contribution at magnetic latitudes  $<60^\circ$  (Hartinger et al., 2023) such as the Continental United  
612 States and Europe.

## 6. Conclusions

The March 2013 St Patrick's Day storm provides a unique opportunity to identify the magnetospheric root causes of the GIC spikes recorded on the Mäntsälä pipeline. The pipeline and other ground-based observatories were in the right place at the right time to capture and quantify the space weather impacts of this storm. The time-frequency perspective provided by wavelet analysis shows spectral features spanning seconds to  $\sim$  hour around the four GICs  $> 10$  A. These multi-scale fluctuations are captured across ground- and space-based observations with different resolutions. Together, CWT and data-fusion of multi-platform observations paint a robust picture of the nature and scale of M-I coupling leading to significant GICs. Based on supporting data and prior MHD modeling, we find that the first 'compound' GIC was likely the result of a mesoscale flow channel interacting with the ring current and the plasmasphere. The interaction manifested in the ionosphere as a transient eastward electrojet closing a partial ring current on the duskside. In only a few minutes the same mesoscale flow channel produced a new FAC structure, strong poleward auroral currents, and a  $> 20$  A change in the pipeline GICs. Two hours later, magnetospheric BBFs created intense small-to-mesoscale ionospheric vortices leading to three periodic spikes, the largest of which was  $> 30$  A. The CWT plot shows significant Pi2 fluctuations, which have been associated with such bursts. Hence, we find substorm injection of varying scales to be the underlying cause of these spikes. Our CWT approach provides a framework for further research on the impact of GICs on different technologies by offering new insights into M-I-ground coupling during geomagnetic storms. With the improved simulation capabilities, we hope to gain a deeper understanding of the GIC drivers. A similar analysis of other GIC events remains in the realm of future work.

635    **Acknowledgments**

636    DJK, BVW, and JLG were partially supported by NSF Award 1933040 and NASA Award  
637    80NSSC20K1784. We gratefully acknowledge the Finnish Meteorological Institute for the GIC  
638    data, IMAGE for NUR magnetometer and 2D equivalent current keogram, SuperMAG and  
639    SuperDARN collaborators, AMPERE team and the Science Data Center for providing data  
640    products derived from the Iridium Communications constellation, enabled by support from the  
641    NSF, TWINS team for ENA data, and OMNIWeb for the solar wind data and derived products.  
642    Special thanks to Ari Viljanen for providing crucial feedback on the ideas and Steve Milan for  
643    providing the IDL code for reference to create FAC keograms. K. Sorathia, M. Wiltberger and R.  
644    Marshall provided useful feedback on our work.

645

## Open Research

Mäntsälä Finnish pipeline ([https://space.fmi.fi/gic/man\\_ascii/](https://space.fmi.fi/gic/man_ascii/)) is used to gather GIC data. The recommended magnetometer data at the NUR station is gathered for the corresponding geomagnetic field ([https://space.fmi.fi/image/www/?page=user\\_defined](https://space.fmi.fi/image/www/?page=user_defined)). SuperMAG is used to generate 90-degree rotated vector plots to give a sense of the auroral electrojet and for the SML, SMR, and SMU indices and sub-indices (<https://supermag.jhuapl.edu/>). Active Magnetosphere and Planetary Electrodynamic Response Experiment (AMPERE) data is used from (<https://ampere.jhuapl.edu/>) for generating Field Aligned Current patterns. The solar wind data is retrieved from OMNIWeb ([https://omniweb.gsfc.nasa.gov/form/omni\\_min.html](https://omniweb.gsfc.nasa.gov/form/omni_min.html)). TWINS data are accessible to the public at <https://cdaweb.gsfc.nasa.gov/>. Fitted SuperDARN data can be downloaded from Globus, instructions of which are provided here: <https://superdarn.ca/data-products>. For supporting information, Defense Meteorological Satellite Program (DMSP) Special Sensor Ultraviolet Spectrographic Imagers (SSUSI) was used to generate plots to understand the spatial distribution of the particle precipitation ([https://ssusi.jhuapl.edu/gal\\_Aur](https://ssusi.jhuapl.edu/gal_Aur)) (Paxton et al., 2002) and other DMSP data was referred from [http://cedar.openmadrigal.org/static/experiments3/2013/dms/17mar13/plots/s16\\_13mar17\\_1.htm](http://cedar.openmadrigal.org/static/experiments3/2013/dms/17mar13/plots/s16_13mar17_1.htm) #20. MetOps2 particle precipitation (Yando et al., 2011) plots were generated using <https://cdaweb.gsfc.nasa.gov/>

## References

- Adhikari, B., Khatiwada, R., & Chapagain, N. P. (2017). Analysis of Geomagnetic Storms Using Wavelet Transforms. *Journal of Nepal Physical Society*, 4(1), 119.  
<https://doi.org/10.3126/jnphysoc.v4i1.17346>
- Anderson, B. J., Takahashi, K., Kamei, T., Waters, C. L., & Toth, B. A. (2002). Birkeland current system key parameters derived from Iridium observations: Method and initial validation results. *Journal of Geophysical Research: Space Physics*, 107(A6).  
<https://doi.org/10.1029/2001JA000080>
- Bao, S., Wang, W., Sorathia, K., Merkin, V., Toffoletto, F., Lin, D., Pham, K., Garretson, J., Wiltberger, M., Lyon, J., & Michael, A. (2023). The Relation Among the Ring Current, Subauroral Polarization Stream, and the Geospace Plume: MAGE Simulation of the 31 March 2001 Super Storm. *Journal of Geophysical Research: Space Physics*, 128(12), e2023JA031923. <https://doi.org/10.1029/2023JA031923>
- Belakhovsky, V., Pilipenko, V., Engebretson, M., Sakharov, Y., & Selivanov, V. (2019). Impulsive disturbances of the geomagnetic field as a cause of induced currents of electric power lines. *Journal of Space Weather and Space Climate*, 9, A18.  
<https://doi.org/10.1051/swsc/2019015>
- Bernhardi, E. H., Cilliers, P. J., & Gaunt, C. T. (2008). Improvement in the modelling of geomagnetically induced currents in southern Africa. *South African Journal of Science*, 104(7–8), 265–272. [http://www.scielo.org.za/scielo.php?script=sci\\_abstract&pid=S0038-23532008000400010&lng=en&nrm=iso&tlng=en](http://www.scielo.org.za/scielo.php?script=sci_abstract&pid=S0038-23532008000400010&lng=en&nrm=iso&tlng=en).
- Boteler, D. H. (1994). Geomagnetically induced currents: Present knowledge and future research. *IEEE Transactions on Power Delivery*, 9(1), 50–58.  
<https://doi.org/10.1109/61.277679>

- Cao, J., Duan, J., Du, A., Ma, Y., Liu, Z., Zhou, G. C., Yang, D., Zhang, T., Li, X., Vellante, M., Reme, H., Dandouras, I., Lucek, E., Carr, C. M., Zong, Q., & Li, Q. (2008). Characteristics of middle- to low-latitude Pi2 excited by bursty bulk flows. *Journal of Geophysical Research: Space Physics*, 113(A7). <https://doi.org/10.1029/2007JA012629>
- Chen, H., Gao, X., Lu, Q., Tsurutani, B. T., & Wang, S. (2020). Statistical Evidence for EMIC Wave Excitation Driven by Substorm Injection and Enhanced Solar Wind Pressure in the Earth's Magnetosphere: Two Different EMIC Wave Sources. *Geophysical Research Letters*, 47(21), e2020GL090275. <https://doi.org/10.1029/2020GL090275>
- Despirak, I. V., Setsko, P. V., Sakharov, Ya. A., Lyubchich, A. A., Selivanov, V. N., & Valev, D. (2022). Observations of Geomagnetic Induced Currents in Northwestern Russia: Case Studies. *Geomagnetism and Aeronomy*, 62(6), 711–723. <https://doi.org/10.1134/S0016793222060032>
- D'Onofrio, M., Partamies, N., & Tanskanen, E. (2014). Eastward electrojet enhancements during substorm activity. *Journal of Atmospheric and Solar-Terrestrial Physics*, 119, 129–137. <https://doi.org/10.1016/j.jastp.2014.07.007>
- Engebretson, M. J., Gaffaney, S. A., Ochoa, J. A., Runov, A., Weygand, J. M., Nishimura, Y., Hartinger, M. D., Pilipenko, V. A., Moldwin, M. B., Connors, M. G., Mann, I. R., Xu, Z., & Rodriguez, J. V. (2024). Signatures of Dipolarizing Flux Bundles in the Nightside Auroral Zone. *Journal of Geophysical Research: Space Physics*, 129(4), e2023JA032266. <https://doi.org/10.1029/2023JA032266>
- Falayi, E. O., Ogunmodimu, O., Bolaji, O. S., Ayanda, J. D., & Ojoniyi, O. S. (2017). Investigation of geomagnetic induced current at high latitude during the storm-time



variation. *NRIAG Journal of Astronomy and Geophysics*, 6(1), 131–140.

<https://doi.org/10.1016/j.nrjag.2017.04.010>

Feldstein, Y. I., Gromova, L. I., Grafe, A., Meng, C.-I., Kalegaev, V. V., Alexeev, I. I., & Sumaruk, Y. P. (1999). Auroral electrojet dynamics during magnetic storms, connection with plasma precipitation and large-scale structure of the magnetospheric magnetic field. *Annales Geophysicae*, 17(4), 497–507. <https://doi.org/10.1007/s00585-999-0497-3>

Feldstein, Y. I., Popov, V. A., Cumnock, J. A., Prigancova, A., Blomberg, L. G., Kozyra, J. U., Tsurutani, B. T., Gromova, L. I., & Levitin, A. E. (2006). Auroral electrojets and boundaries of plasma domains in the magnetosphere during magnetically disturbed intervals. *Annales Geophysicae*, 24(8), 2243–2276. <https://doi.org/10.5194/angeo-24-2243-2006>

Ferdousi, B., Nishimura, Y., Maruyama, N., & Lyons, L. R. (2019). Subauroral Neutral Wind Driving and Its Feedback to SAPS During the 17 March 2013 Geomagnetic Storm. *Journal of Geophysical Research: Space Physics*, 124(3), 2323–2337. <https://doi.org/10.1029/2018JA026193>

Gannon, J. L., Birchfield, A. B., Shetye, K. S., & Overbye, T. J. (2017). A Comparison of Peak Electric Fields and GICs in the Pacific Northwest Using 1-D and 3-D Conductivity. *Space Weather*, 15(11), 1535–1547. <https://doi.org/10.1002/2017SW001677>

Ganushkina, N., Jaynes, A., & Liemohn, M. (2017). Space Weather Effects Produced by the Ring Current Particles. *Space Science Reviews*, 212(3), 1315–1344. <https://doi.org/10.1007/s11214-017-0412-2>

Gkioulidou, M., Ukhorskiy, A. Y., Mitchell, D. G., Sotirelis, T., Mauk, B. H., & Lanzerotti, L. J. (2014). The role of small-scale ion injections in the buildup of Earth's ring current

pressure: Van Allen Probes observations of the 17 March 2013 storm. *Journal of Geophysical Research: Space Physics*, 119(9), 7327–7342.

<https://doi.org/10.1002/2014JA020096>

Goldstein, J., Valek, P., McComas, D. J., & Redfern, J. (2012). TWINS energetic neutral atom observations of local-time-dependent ring current anisotropy. *Journal of Geophysical Research: Space Physics*, 117(A11). <https://doi.org/10.1029/2012JA017804>

Goldstein, J., Valek, P. W., McComas, D. J., Redfern, J., Spence, H., Skoug, R. M., Larsen, B. A., D. Reeves, G., & Nakamura, R. (2020). Global ENA Imaging and In Situ Observations of Substorm Dipolarization on 10 August 2016. *Journal of Geophysical Research: Space Physics*, 125(4), e2019JA027733. <https://doi.org/10.1029/2019JA027733>

Grafe, A., Bessalov, P. A., Trakhtengerts, V. Y., & Demekhov, A. G. (1997). *Afternoon mid-latitude current system and low-latitude geomagnetic field asymmetry during geomagnetic storms*.

Grawe, M. A., & Makela, J. J. (2021). Predictability of Geomagnetically Induced Currents as a Function of Available Magnetic Field Information. *Space Weather*, 19(8), e2021SW002747. <https://doi.org/10.1029/2021SW002747>

Greenwald, R. A., Baker, K. B., Dudeney, J. R., Pinnock, M., Jones, T. B., Thomas, E. C., Villain, J.-P., Cerisier, J.-C., Senior, C., Hanuise, C., Hunsucker, R. D., Sofko, G., Koehler, J., Nielsen, E., Pellinen, R., Walker, A. D. M., Sato, N., & Yamagishi, H. (1995). DARN/SuperDARN. *Space Science Reviews*, 71(1), 761–796.

<https://doi.org/10.1007/BF00751350>

756 Grinsted, A., Moore, J. C., & Jevrejeva, S. (2004). Application of the cross wavelet transform  
757 and wavelet coherence to geophysical time series. *Nonlinear Processes in Geophysics*,  
758 11(5/6), 561–566. <https://doi.org/10.5194/npg-11-561-2004>

759 Hall, D. L., & Llinas, J. (1997). *An Introduction to Multisensor Data Fusion*.  
760 <https://doi.org/10.1109/5.554205>

761 Hartinger, M. D., Shi, X., Rodger, C. J., Fujii, I., Rigler, E. J., Kappler, K., Matzka, J., Love, J. J.,  
762 Baker, J. B. H., Mac Manus, D. H., Dalzell, M., & Petersen, T. (2023). Determining ULF  
763 Wave Contributions to Geomagnetically Induced Currents: The Important Role of  
764 Sampling Rate. *Space Weather*, 21(5), e2022SW003340.  
765 <https://doi.org/10.1029/2022SW003340>

766 Heyns, M. J., Lotz, S. I., & Gaunt, C. T. (2021). Geomagnetic Pulsations Driving  
767 Geomagnetically Induced Currents. *Space Weather*, 19(2), e2020SW002557.  
768 <https://doi.org/10.1029/2020SW002557>

769 Hubert, B., Kauristie, K., Amm, O., Milan, S. E., Grocott, A., Cowley, S. W. H., & Pulkkinen, T.  
770 I. (2007). Auroral streamers and magnetic flux closure. *Geophysical Research Letters*,  
771 34(15). <https://doi.org/10.1029/2007GL030580>

772 Iijima, T., & Potemra, T. A. (1976). The amplitude distribution of field-aligned currents at  
773 northern high latitudes observed by Triad. *Journal of Geophysical Research*, 81(13),  
774 2165–2174. <https://onlinelibrary.wiley.com/doi/abs/10.1029/JA081i013p02165>

775 Juusola, L., Nakamura, R., Amm, O., & Kauristie, K. (2009). Conjugate ionospheric equivalent  
776 currents during bursty bulk flows. *Journal of Geophysical Research: Space Physics*,  
777 114(A4). <https://doi.org/10.1029/2008JA013908>

778 Juusola, L., Viljanen, A., Dimmock, A. P., Kellinsalmi, M., Schillings, A., & Weygand, J. M.  
 779 (2023). Drivers of rapid geomagnetic variations at high latitudes. *Annales Geophysicae*,  
 780 41(1), 13–37. <https://doi.org/10.5194/angeo-41-13-2023>  
 781 Kamide, Y., & Fukushima, N. (1972). POSITIVE GEOMAGNETIC BAYS IN EVENING HIGH  
 782 LATITUDES AND THEIR POSSIBLE CONNECTION WITH PARTIAL RING  
 783 CURRENT. *Rep. Ionosphere Space Res. Jap.* 26: No. 1-2, 79-101(1972).  
 784 <https://www.osti.gov/biblio/4643131>  
 785 Keiling, A., Angelopoulos, V., Runov, A., Weygand, J., Apatenkov, S. V., Mende, S., McFadden,  
 786 J., Larson, D., Amm, O., Glassmeier, K.-H., & Auster, H. U. (2009). Substorm current  
 787 wedge driven by plasma flow vortices: THEMIS observations. *Journal of Geophysical*  
 788 *Research: Space Physics*, 114(A1). <https://doi.org/10.1029/2009JA014114>  
 789 Kepko, L., & Kivelson, M. (1999). Generation of Pi2 pulsations by bursty bulk flows. *Journal of*  
 790 *Geophysical Research: Space Physics*, 104(A11), 25021–25034.  
 791 <https://doi.org/10.1029/1999JA900361>  
 792 Kepko, L., Kivelson, M. G., & Yumoto, K. (2001). Flow bursts, braking, and Pi2 pulsations.  
 793 *Journal of Geophysical Research: Space Physics*, 106(A2), 1903–1915.  
 794 <https://doi.org/10.1029/2000JA000158>  
 795 Khanal, K., Adhikari, B., Chapagain, N. P., & Bhattarai, B. (2019). HILDCAA-Related GIC and  
 796 Possible Corrosion Hazard in Underground Pipelines: A Comparison Based on Wavelet  
 797 Transform. *Space Weather*, 17(2), 238–251. <https://doi.org/10.1029/2018SW001879>  
 798 King, J. H., & Papitashvili, N. E. (2005). Solar wind spatial scales in and comparisons of hourly  
 799 Wind and ACE plasma and magnetic field data. *Journal of Geophysical Research: Space*  
 800 *Physics*, 110(A2). <https://doi.org/10.1029/2004JA010649>

801 Krall, J., Huba, J. D., & Sazykin, S. (2017). Erosion of the plasmasphere during a storm. *Journal*  
802 *of Geophysical Research: Space Physics*, 122(9), 9320–9328.  
803 <https://doi.org/10.1002/2017JA024450>

804 Lin, D., Sorathia, K., Wang, W., Merkin, V., Bao, S., Pham, K., Wiltberger, M., Shi, X.,  
805 Toffoletto, F., Michael, A., Lyon, J., Garretson, J., & Anderson, B. (2021). The Role of  
806 Diffuse Electron Precipitation in the Formation of Subauroral Polarization Streams.  
807 *Journal of Geophysical Research: Space Physics*, 126(12), e2021JA029792.  
808 <https://doi.org/10.1029/2021JA029792>

809 Lyons, L. R., Gallardo-Lacourt, B., Zou, S., Weygand, J. M., Nishimura, Y., Li, W., Gkioulidou,  
810 M., Angelopoulos, V., Donovan, E. F., Ruohoniemi, J. M., Anderson, B. J., Shepherd, S.  
811 G., & Nishitani, N. (2016). The 17 March 2013 storm: Synergy of observations related to  
812 electric field modes and their ionospheric and magnetospheric Effects. *Journal of*  
813 *Geophysical Research: Space Physics*, 121(11). <https://doi.org/10.1002/2016JA023237>

814 Lysak, R. L., Song, Y., Sciffer, M. D., & Waters, C. L. (2015). Propagation of Pi2 pulsations in a  
815 dipole model of the magnetosphere. *Journal of Geophysical Research: Space Physics*,  
816 120(1), 355–367. <https://doi.org/10.1002/2014JA020625>

817 Marshall, R. A., Dalzell, M., Waters, C. L., Goldthorpe, P., & Smith, E. A. (2012).  
818 Geomagnetically induced currents in the New Zealand power network. *Space Weather*,  
819 10(8). <https://doi.org/10.1029/2012SW000806>

820 Marshall, R. A., Kelly, A., Van Der Walt, T., Honecker, A., Ong, C., Mikkelsen, D., Spierings, A.,  
821 Ivanovich, G., & Yoshikawa, A. (2017). Modeling geomagnetic induced currents in  
822 Australian power networks. *Space Weather*, 15(7), 895–916.  
823 <https://doi.org/10.1002/2017SW001613>

824 McComas, D. J., Allegrini, F., Baldonado, J., Blake, B., Brandt, P. C., Burch, J., Clemmons, J.,  
825 Crain, W., Delapp, D., DeMajistre, R., Everett, D., Fahr, H., Friesen, L., Funsten, H.,  
826 Goldstein, J., Gruntman, M., Harbaugh, R., Harper, R., Henkel, H., ... Zoennchen, J.  
827 (2009). The Two Wide-angle Imaging Neutral-atom Spectrometers (TWINS) NASA  
828 Mission-of-Opportunity. *Space Science Reviews*, 142(1), 157–231.  
829 <https://doi.org/10.1007/s11214-008-9467-4>

830 McComas, D. J., Buzulukova, N., Connors, M. G., Dayeh, M. A., Goldstein, J., Funsten, H. O.,  
831 Fuselier, S., Schwadron, N. A., & Valek, P. (2012). Two Wide-Angle Imaging Neutral-  
832 Atom Spectrometers and Interstellar Boundary Explorer energetic neutral atom imaging  
833 of the 5 April 2010 substorm. *Journal of Geophysical Research: Space Physics*, 117(A3).  
834 <https://doi.org/10.1029/2011JA017273>

835 Milling, D. K., Rae, I. J., Mann, I. R., Murphy, K. R., Kale, A., Russell, C. T., Angelopoulos, V.,  
836 & Mende, S. (2008). Ionospheric localisation and expansion of long-period Pi1 pulsations  
837 at substorm onset. *Geophysical Research Letters*, 35(17).  
838 <https://doi.org/10.1029/2008GL033672>

839 Mishin, E., Nishimura, Y., & Foster, J. (2017). SAPS/SAID revisited: A causal relation to the  
840 substorm current wedge. *Journal of Geophysical Research: Space Physics*, 122(8), 8516–  
841 8535. <https://doi.org/10.1002/2017JA024263>

842 Newell, P. T., & Gjerloev, J. W. (2011). Evaluation of SuperMAG auroral electrojet indices as  
843 indicators of substorms and auroral power. *Journal of Geophysical Research: Space*  
844 *Physics*, 116(A12). <https://doi.org/10.1029/2011JA016779>

845 Newell, P. T., & Gjerloev, J. W. (2012). SuperMAG-based partial ring current indices. *Journal of*  
846 *Geophysical Research: Space Physics*, 117(A5). <https://doi.org/10.1029/2012JA017586>

847 Newell, P. T., Sotirelis, T., Liou, K., Meng, C.-I., & Rich, F. J. (2007). A nearly universal solar  
 848 wind-magnetosphere coupling function inferred from 10 magnetospheric state variables.  
 849 *Journal of Geophysical Research: Space Physics*, 112(A1).  
 850 <https://doi.org/10.1029/2006JA012015>

851 Nosé, M., Iyemori, T., Wang, L., Hitchman, A., Matzka, J., Feller, M., Egdorf, S., Gilder, S.,  
 852 Kumasaka, N., Koga, K., Matsumoto, H., Koshiishi, H., Cifuentes-Nava, G., Curto, J. J.,  
 853 Segarra, A., & Çelik, C. (2012). Wp index: A new substorm index derived from high-  
 854 resolution geomagnetic field data at low latitude. *Space Weather*, 10(8).  
 855 <https://doi.org/10.1029/2012SW000785>

856 Orr, L., Chapman, S. C., & Beggan, C. D. (2021). Wavelet and Network Analysis of Magnetic  
 857 Field Variation and Geomagnetically Induced Currents During Large Storms. *Space*  
 858 *Weather*, 19(9), e2021SW002772. <https://doi.org/10.1029/2021SW002772>

859 Palin, L., Opgenoorth, H. J., Ågren, K., Zivkovic, T., Sergeev, V. A., Kubyshkina, M. V.,  
 860 Nikolaev, A., Kauristie, K., van de Kamp, M., Amm, O., Milan, S. E., Imber, S. M.,  
 861 Facskó, G., Palmroth, M., & Nakamura, R. (2016). Modulation of the substorm current  
 862 wedge by bursty bulk flows: 8 September 2002—Revisited. *Journal of Geophysical*  
 863 *Research: Space Physics*, 121(5), 4466–4482. <https://doi.org/10.1002/2015JA022262>

864 Paxton, L. J., Morrison, D., Zhang, Y., Kil, H., Wolven, B., Ogorzalek, B. S., Humm, D. C., &  
 865 Meng, C.-I. (2002). Validation of remote sensing products produced by the Special  
 866 Sensor Ultraviolet Scanning Imager (SSUSI): A far UV-imaging spectrograph on DMSP  
 867 F-16. *Optical Spectroscopic Techniques, Remote Sensing, and Instrumentation for*  
 868 *Atmospheric and Space Research IV*, 4485, 338–348. <https://doi.org/10.1117/12.454268>

869 Potapov, A., Dovbnya, B., Baishev, D., Rahmatulin, R., & Polyushkina, T. (2017). Narrow-band  
870 emission with 0.5 to 3.5 Hz varying frequency in the background of the main phase of the  
871 17 March 2013 magnetic storm. *Solar-Terrestrial Physics*, 2, 16–30.  
872 <https://doi.org/10.12737/24271>

873 Pulkkinen, A., Bernabeu, E., Thomson, A., Viljanen, A., Pirjola, R., Boteler, D., Eichner, J.,  
874 Cilliers, P. J., Welling, D., Savani, N. P., Weigel, R. S., Love, J. J., Balch, C., Ngwira, C.  
875 M., Crowley, G., Schultz, A., Kataoka, R., Anderson, B., Fugate, D., ... MacAlester, M.  
876 (2017). Geomagnetically induced currents: Science, engineering, and applications  
877 readiness. *Space Weather*, 15(7), 828–856. <https://doi.org/10.1002/2016SW001501>

878 Pulkkinen, A., & Kataoka, R. (2006). S-transform view of geomagnetically induced currents  
879 during geomagnetic superstorms. *Geophysical Research Letters*, 33(12).  
880 <https://doi.org/10.1029/2006GL025822>

881 Pulkkinen, A., Lindahl, S., Viljanen, A., & Pirjola, R. (2005). Geomagnetic storm of 29–31  
882 October 2003: Geomagnetically induced currents and their relation to problems in the  
883 Swedish high-voltage power transmission system. *Space Weather*, 3(8).  
884 <https://doi.org/10.1029/2004SW000123>

885 Pulkkinen, A., Pirjola, R., Boteler, D., Viljanen, A., & Yegorov, I. (2001). Modelling of space  
886 weather effects on pipelines. *Journal of Applied Geophysics*, 48(4), 233–256.  
887 [https://doi.org/10.1016/S0926-9851\(01\)00109-4](https://doi.org/10.1016/S0926-9851(01)00109-4)

888 Pulkkinen, A., Viljanen, A., Pajunpää, K., & Pirjola, R. (2001). Recordings and occurrence of  
889 geomagnetically induced currents in the Finnish natural gas pipeline network. *Journal of*  
890 *Applied Geophysics*, 48(4), 219–231. [https://doi.org/10.1016/S0926-9851\(01\)00108-2](https://doi.org/10.1016/S0926-9851(01)00108-2)



891 Saito, T. (1969). Geomagnetic pulsations. *Space Science Reviews*, 10(3), 319–412.  
892 <https://doi.org/10.1007/BF00203620>

893 Sciola, A., Merkin, V. G., Sorathia, K., Gkioulidou, M., Bao, S., Toffoletto, F., Pham, K., Lin, D.,  
894 Michael, A., Wiltberger, M., & Ukhorskiy, A. (2023). The Contribution of Plasma Sheet  
895 Bubbles to Stormtime Ring Current Buildup and Evolution of Its Energy Composition.  
896 *Journal of Geophysical Research: Space Physics*, 128(11), e2023JA031693.  
897 <https://doi.org/10.1029/2023JA031693>

898 Slavič, J., Simonovski, I., & Boltežar, M. (2003). Damping identification using a continuous  
899 wavelet transform: Application to real data. *Journal of Sound and Vibration*, 262(2), 291–  
900 307. [https://doi.org/10.1016/S0022-460X\(02\)01032-5](https://doi.org/10.1016/S0022-460X(02)01032-5)

901 Søråas, F., Sandanger, M. I., & Smith-Johnsen, C. (2018). NOAA POES and MetOp particle  
902 observations during the 17 March 2013 storm. *Journal of Atmospheric and Solar-*  
903 *Terrestrial Physics*, 177, 115–124. <https://doi.org/10.1016/j.jastp.2017.09.004>

904 Sorathia, K. A., Michael, A., Merkin, V. G., Ohtani, S., Keese, A. M., Sciola, A., Lin, D.,  
905 Garretson, J., Ukhorskiy, A. Y., Bao, S., Roedig, C. B., & Pulkkinen, A. (2023).  
906 Multiscale Magnetosphere-Ionosphere Coupling During Stormtime: A Case Study of the  
907 Dawnside Current Wedge. *Journal of Geophysical Research: Space Physics*, 128(11),  
908 e2023JA031594. <https://doi.org/10.1029/2023JA031594>

909 Sorathia, K. A., Ukhorskiy, A. Y., Merkin, V. G., Fennell, J. F., & Claudepierre, S. G. (2018).  
910 Modeling the Depletion and Recovery of the Outer Radiation Belt During a Geomagnetic  
911 Storm: Combined MHD and Test Particle Simulations. *Journal of Geophysical Research:*  
912 *Space Physics*, 123(7), 5590–5609. <https://doi.org/10.1029/2018JA025506>

913 Spasojevic, M., & Fuselier, S. A. (2009). Temporal evolution of proton precipitation associated  
 914 with the plasmaspheric plume. *Journal of Geophysical Research: Space Physics*,  
 915 114(A12). <https://doi.org/10.1029/2009JA014530>  
 916 Tanskanen, E. I. (2009). A comprehensive high-throughput analysis of substorms observed by  
 917 IMAGE magnetometer network: Years 1993–2003 examined. *Journal of Geophysical*  
 918 *Research: Space Physics*, 114(A5). <https://doi.org/10.1029/2008JA013682>  
 919 Torrence, C., & Compo, G. P. (1998). A Practical Guide to Wavelet Analysis. *Bulletin of the*  
 920 *American Meteorological Society*, 79(1), 61–78. [https://doi.org/10.1175/1520-](https://doi.org/10.1175/1520-0477(1998)079<0061:APGTWA>2.0.CO;2)  
 921 0477(1998)079<0061:APGTWA>2.0.CO;2  
 922 Trakhtengerts, V. Y., & Demekhov, A. G. (2005). Discussion paper: Partial ring current and  
 923 polarization jet. *International Journal of Geomagnetism and Aeronomy*, 5, G13007.  
 924 <https://doi.org/10.1029/2004GI000091>  
 925 Tsurutani, B. T., & Hajra, R. (2021). The Interplanetary and Magnetospheric causes of  
 926 Geomagnetically Induced Currents (GICs) > 10 A in the Mäntsälä Finland Pipeline: 1999  
 927 through 2019. *Journal of Space Weather and Space Climate*, 11, 23.  
 928 <https://doi.org/10.1051/swsc/2021001>  
 929 Verkhoglyadova, O. P., Tsurutani, B. T., Mannucci, A. J., Mlynczak, M. G., Hunt, L. A., Paxton,  
 930 L. J., & Komjathy, A. (2016). Solar wind driving of ionosphere-thermosphere responses  
 931 in three storms near St. Patrick's Day in 2012, 2013, and 2015. *Journal of Geophysical*  
 932 *Research: Space Physics*, 121(9), 8900–8923. <https://doi.org/10.1002/2016JA022883>  
 933 Viljanen, A., Pulkkinen, A., Pirjola, R., Pajunpää, K., Posio, P., & Koistinen, A. (2006).  
 934 Recordings of geomagnetically induced currents and a nowcasting service of the Finnish

935 natural gas pipeline system. *Space Weather*, 4(10).

936 <https://doi.org/10.1029/2006SW000234>

937 Watari, S., Kunitake, M., Kitamura, K., Hori, T., Kikuchi, T., Shiokawa, K., Nishitani, N.,

938 Kataoka, R., Kamide, Y., Aso, T., Watanabe, Y., & Tsuneta, Y. (2009). Measurements of

939 geomagnetically induced current in a power grid in Hokkaido, Japan. *Space Weather*,

940 7(3), 2008SW000417. <https://doi.org/10.1029/2008SW000417>

941 Waters, C. L., Anderson, B. J., & Liou, K. (2001). Estimation of global field aligned currents

942 using the iridium® System magnetometer data. *Geophysical Research Letters*, 28(11),

943 2165–2168. <https://doi.org/10.1029/2000GL012725>

944 Waters, C. L., Gjerloev, J. W., Dupont, M., & Barnes, R. J. (2015). Global maps of ground

945 magnetometer data. *Journal of Geophysical Research: Space Physics*, 120(11), 9651–

946 9660. <https://doi.org/10.1002/2015JA021596>

947 Wei, D., Dunlop, M. W., Yang, J., Dong, X., Yu, Y., & Wang, T. (2021). Intense  $dB/dt$  Variations

948 Driven by Near-Earth Bursty Bulk Flows (BBFs): A Case Study. *Geophysical Research*

949 *Letters*, 48(4), e2020GL091781. <https://doi.org/10.1029/2020GL091781>

950 Wiltberger, M., Merkin, V., Zhang, B., Toffoletto, F., Oppenheim, M., Wang, W., Lyon, J. G.,

951 Liu, J., Dimant, Y., Sitnov, M. I., & Stephens, G. K. (2017). Effects of electrojet

952 turbulence on a magnetosphere-ionosphere simulation of a geomagnetic storm. *Journal of*

953 *Geophysical Research: Space Physics*, 122(5), 5008–5027.

954 <https://doi.org/10.1002/2016JA023700>

955 Wu, C.-C., Liou, K., Vourlidas, A., Plunkett, S., Dryer, M., Wu, S. T., & Mewaldt, R. A. (2016).

956 Global magnetohydrodynamic simulation of the 15 March 2013 coronal mass ejection

event—Interpretation of the 30–80 MeV proton flux. *Journal of Geophysical Research: Space Physics*, 121(1), 56–76. <https://doi.org/10.1002/2015JA021051>

Xu, W.-H., Xing, Z.-Y., Balan, N., Liang, L.-K., Wang, Y.-L., Zhang, Q.-H., Sun, Z.-D., & Li, W.-B. (2022). Spectral analysis of geomagnetically induced current and local magnetic field during the 17 March 2013 geomagnetic storm. *Advances in Space Research*, 69(9), 3417–3425. <https://doi.org/10.1016/j.asr.2022.02.025>

Xu, Z. (2011). *Study of Geomagnetic Disturbances and Ring Current Variability During Storm and Quiet Times Using Wavelet Analysis and Ground-Based Magnetic Data from Multiple Stations* [Utah State University]. <https://digitalcommons.usu.edu/etd/984>

Xu, Z., Hartinger, M. D., Clauer, C. R., Peek, T., & Behlke, R. (2017). A comparison of the ground magnetic responses during the 2013 and 2015 St. Patrick’s Day geomagnetic storms. *Journal of Geophysical Research: Space Physics*, 122(4), 4023–4036. <https://doi.org/10.1002/2016JA023338>

Yando, K., Millan, R. M., Green, J. C., & Evans, D. S. (2011). A Monte Carlo simulation of the NOAA POES Medium Energy Proton and Electron Detector instrument. *Journal of Geophysical Research: Space Physics*, 116(A10). <https://doi.org/10.1029/2011JA016671>

Yang, J., Toffoletto, F. R., Wolf, R. A., Sazykin, S., Ontiveros, P. A., & Weygand, J. M. (2012). Large-scale current systems and ground magnetic disturbance during deep substorm injections. *Journal of Geophysical Research: Space Physics*, 117(A4). <https://doi.org/10.1029/2011JA017415>

Yiou, P., Baert, E., & Loutre, M. F. (1996). Spectral analysis of climate data. *Surveys in Geophysics*, 17(6), 619–663. <https://doi.org/10.1007/BF01931784>

979 Yu, Y., Cao, J., Fu, H., Lu, H., & Yao, Z. (2017). The effects of bursty bulk flows on global-scale  
980 current systems. *Journal of Geophysical Research: Space Physics*, 122(6), 6139–6149.  
981 <https://doi.org/10.1002/2017JA024168>

982 Yu, Y., Cao, J., Pu, Z., Jordanova, V. K., & Ridley, A. (2022). Meso-Scale Electrodynamic  
983 Coupling of the Earth Magnetosphere-Ionosphere System. *Space Science Reviews*,  
984 218(8), 74. <https://doi.org/10.1007/s11214-022-00940-0>

985 Yu, Y., Jordanova, V., Welling, D., Larsen, B., Claudepierre, S. G., & Kletzing, C. (2014). The  
986 role of ring current particle injections: Global simulations and Van Allen Probes  
987 observations during 17 March 2013 storm. *Geophysical Research Letters*, 41(4), 1126–  
988 1132. <https://doi.org/10.1002/2014GL059322>

989 Zou, Y., Dowell, C., Ferdousi, B., Lyons, L. R., & Liu, J. (2022). Auroral Drivers of Large dB/dt  
990 During Geomagnetic Storms. *Space Weather*, 20(11), e2022SW003121.  
991 <https://doi.org/10.1029/2022SW003121>